A systematic analysis of the human immune response to Plasmodium vivax

A systematic analysis of the human immune response to *Plasmodium vivax*

Florian A. Bach,[1*] Diana Muñoz Sandoval,[1,2] Michalina Mazurczyk,[3] Yrene Themistocleous,[4] Thomas A. Rawlinson,[4] Adam C. Harding,[1] Alison Kemp,[5] Sarah E. Silk,[4,6] Jordan R. Barrett,[4,6] Nick J. Edwards,[4] Alasdair Ivens,[1] Julian C. Rayner,[5] Angela M. Minassian,[4,6] Giorgio Napolitani,[3] Simon J. Draper,[4,6] Philip J. Spence[1*]

[1]Institute of Immunology and Infection Research, University of Edinburgh, UK. [2]Instituto de Microbiologia, Universidad San Francisco de Quito, Ecuador. [3]MRC Human Immunology Unit, Weatherall Institute of Molecular Medicine, University of Oxford, UK. [4]The Jenner Institute, University of Oxford, UK. [5]Cambridge Institute for Medical Research, University of Cambridge, UK. [6]Department of Biochemistry, University of Oxford, UK.

[*]correspondence:

fbach@stanford.edu | tel. +1 (650) 724 5343 | ORCID ID 0000-0002-0126-5516
240 Pasteur Drive, Biomedical Innovation Building, 94304 Palo Alto, California, USA.

pspence@ed.ac.uk | tel. +44 (0) 131 650 7315 | ORCID ID 0000-0002-5506-2773
Ashworth Laboratories, Charlotte Auerbach Road, Edinburgh, EH9 3FL, UK.

declaration: Yrene Themistocleous is a contributor to intellectual property licenced by Oxford University Innovation to AstraZeneca. All other authors have declared that no conflict of interest exists.

Abstract

Background

The biology of *Plasmodium vivax* is markedly different to that of *P. falciparum*; how this shapes the immune response to infection remains unclear. To address this shortfall, we inoculated human volunteers with a clonal field isolate of *P. vivax* and tracked their response through infection and convalescence.

Methods

Participants were injected intravenously with blood-stage parasites and infection dynamics were tracked in real-time by quantitative PCR. Whole blood samples were used for high dimensional protein analysis, RNA-sequencing and Cytometry by Time Of Flight (CyTOF), and temporal changes in the host response to *P. vivax* were quantified by linear regression. Comparative analyses with *P. falciparum* were then undertaken using analogous datasets derived from prior controlled human malaria infection studies.

Results

P. vivax rapidly induced a type I inflammatory response that coincided with hallmark features of clinical malaria. This acute phase response shared remarkable overlap with that induced by *P. falciparum* but was significantly elevated (at RNA and protein level) leading to an increased incidence of pyrexia. In contrast, T cell activation and terminal differentiation was significantly increased in volunteers infected with *P. falciparum*. Heterogeneous $CD4^+$ T cells were found to dominate this adaptive response and phenotypic analysis revealed unexpected features normally associated with cytotoxicity and autoinflammatory disease.

Conclusion

P. vivax triggers increased systemic interferon signaling (cf *P. falciparum*), which likely explains its reduced pyrogenic threshold. In contrast, *P. falciparum* drives T cell activation far in excess of *P. vivax*, which may partially explain why falciparum malaria more frequently causes severe disease.

Trial registration

ClinicalTrials.gov NCT03797989.

Funding

Supported by the European Union's Horizon 2020 Research and Innovation programme, the Wellcome Trust and the Royal Society.

Introduction

Plasmodium vivax causes more than half of all malaria cases in the Americas and South-East Asia (1) and its distinct biology (cf *P. falciparum*) presents unique challenges for control and elimination. Dormant liver-stage parasites can trigger multiple relapses over many months or years (2); asexual blood-stage parasites preferentially accumulate in the spleen to promote chronic infection (3); and gametocytes develop rapidly within the bone marrow to maximise transmission (4). Total pathogen load is nevertheless reduced compared to *P. falciparum* and severe disease is a much less common outcome of infection (5). This may be explained in part by *P. vivax* invading $CD71^{+}$ reticulocytes (as opposed to mature red cells) and sequestering far less effectively than *P. falciparum* (6, 7). But parasite virulence may also be influenced by the host response to infection (8). It is well established that the pyrogenic threshold is far lower for *P. vivax* (indicating differential regulation of the acute phase response) and that clinical immunity (leading to asymptomatic infection) is acquired much more quickly (9-13). Parasite species may therefore regulate the immune response to shape the discrete patterns of disease observed in human malaria.

There are large gaps in our understanding of the immune response to *P. vivax* compared to the better studied *P. falciparum* (14). We know the *P. vivax* genome is enriched in CpG motifs that can bind TLR9 to trigger type I interferon production (15, 16) and that monocytes and neutrophils are highly phagocytic (and generate reactive oxygen species) during acute infection (17, 18). We also know that by invading reticulocytes (which express class I MHC) *P. vivax* may offer an alternative route to pathogen control - cytolysis by antigen-specific $CD8^{+}$ T cells (19). Nevertheless, a systematic analysis of the immune response to *P. vivax* is lacking; we have limited information on the number or function of activated T cells *in vivo*; and field studies that directly compare the host response between *P. vivax* and *P. falciparum* are few and far between. These studies are extremely challenging in an endemic setting due to differences in host age, pathogen load, parasite genotype and history of exposure. However, the resurgence of human challenge models (20-22) provides a unique opportunity to compare the immune response to these evolutionarily divergent parasites (23) whilst accounting for these important confounders.

Controlled human malaria infection (CHMI) has thus far shown that *P. vivax* triggers a systemic interferon-stimulated response (24) and activates the kynurenine pathway (likely through induction of IDO) (25). To build upon these findings we generated a new cryopreserved stabilate of *P. vivax* suitable for CHMI (26) and used systems biology tools to map the immune response at unprecedented resolution. We then reasoned that a direct comparison with the host response to *P. falciparum* may shed new light on why falciparum malaria more frequently causes severe disease and why *P. vivax* is better able to induce rapid clinical immunity.

Results

Plasmodium vivax triggers interferon-stimulated inflammation

Six malaria-naive volunteers were infected with *P. vivax* (clone PvW1) by direct blood challenge (Supplemental File 1). These cryopreserved parasites originate from a naturally-infected donor in Thailand and have been reset by mosquito transmission (see (26) for details). All volunteers reached the treatment threshold (5,000 or 10,000 parasite genome copies ml^{-1} with or without symptoms, respectively) within 12-16 days of inoculation (Figure 1A-B). Whole blood samples were taken at baseline (day before challenge), during infection (C7 for 7-days post-challenge), at the peak of infection (diagnosis), after drug treatment (T6 for 6-days post-treatment) and 45-days after challenge (memory time-point). The majority of adverse events (including symptomatology, haematology and blood chemistry) peaked within 24-hours of treatment. Notably, all volunteers exhibited pronounced lymphopenia (Figure 1C), serum transaminases were elevated in 5 of 6 volunteers indicating liver injury (Figure 1D) and pyrexia was a common outcome of infection (26).

Next, we sought to capture the acute phase response to *P. vivax* by quantifying 39 plasma analytes using a custom bead-based protein assay. To identify analytes that varied significantly through time we fit linear regression models for each analyte in the form of analyte~timepoint+volunteer using log10 transformed concentrations and time-point as a categorical variable. After correcting for multiple testing, we found 12 analytes with an FDR < 0.05 (Figure 1E). All significant analytes increased in abundance and peaked at diagnosis (except IL-18, which peaked at T6). The analyte with the lowest FDR was IFNγ indicating a robust type I inflammatory response, which has been extensively described in febrile disease (inc. vivax malaria (24, 25, 27)). In agreement, analytes associated with the recruitment (CCL2, CXCL9 and CXCL10) and activation (IL-12, IL-18 and IL-21) of inflammatory monocytes and $CD4^+$ T cells were also induced. And furthermore, D-Dimer (a biomarker of intravascular fibrinolysis that is intimately linked to systemic inflammation (28)) was significantly increased. All analytes had returned to baseline levels by 45-days post-challenge. Collectively, these data demonstrate that *P. vivax* triggers a type I inflammatory response that coincides with hallmark features of clinical malaria including lymphopenia, pyrexia and fibrinolysis. Importantly, symptoms and plasma analytes rapidly return to baseline levels after parasite clearance with the exception of IL-18 and ALT, which peak six days after drug treatment.

Inflammation is followed by proliferation in peripheral blood

To further characterise the systemic response to *P. vivax* we used bulk RNA-sequencing to resolve changes in whole blood gene expression through time. We first grouped samples by time-point and then used DESeq2 (29) to perform pairwise

comparisons with baseline samples. In this way, we could identify changes in gene expression that were shared across the volunteer cohort, and we used an adjusted p value < 0.05 for significance. To take into account the drop in lymphocytes at diagnosis we performed differential blood counts, which revealed that myeloid cells increased by 13.6% at the peak of infection (Figure 2A). We therefore only considered significant genes with an absolute fold-change > 1.5 so that differential expression could not merely be explained by lymphopenia (assuming myeloid/lymphoid cells share similar transcriptional activity). Using these two thresholds we found that the transcriptional response peaked at diagnosis with 2221 differentially expressed genes (DEG). Of note, there were no DEG prior to diagnosis indicating that *P. vivax* does not induce detectable changes in gene expression when infection is sub-patent (below 5,000 to 10,000 parasites ml^{-1}). This is in line with previous observations (24). The number of DEG dropped to 298 at T6 and surprisingly most of these were unique to this time-point, suggesting that a distinct transcriptional response follows drug treatment.

To directly compare the biological functions of the host response at diagnosis and T6 we used gene ontology (GO) network analysis. ClueGO assigns significant GO terms based on differential gene expression and then groups them into functional networks by relatedness (30, 31). The transcriptional response at diagnosis was dominated by upregulation of innate signaling and defence pathways, including GO terms associated with NF-κB signaling, leukocyte migration and cytokine production (Figure 2B). On the other hand, the GO terms unique to T6 related to chromatin remodeling and cell cycle progression rather than inflammation (Figure 2C). When we looked at the signature genes associated with these diverging networks we found that the top hits at diagnosis were downstream targets of interferon signaling and critical regulators of host metabolism and T cell activation (for example, IDO and PDL1) (Figure 2D). Importantly, many of these genes have been shown to be upregulated in purified monocytes and neutrophils isolated from *P. vivax* infected patients (17, 18). In contrast, the top DEG after drug treatment included regulators of nuclear division and proliferation. This gene signature is unlikely to derive from activated myeloid cells, which are terminally differentiated and do not proliferate in peripheral blood. Instead, these data suggest that we are capturing activated lymphocytes as they return to the circulation six days after parasite clearance.

Proliferation coincides with the appearance of activated T cells

It is well known that T cells are recruited out of circulation during infection and activated within the inflamed spleen (32, 33); by studying their phenotype as they re-enter peripheral blood it may be possible to examine T cell priming and (by extension) the tissue environment in human malaria. To explore this idea we leveraged CyTOF to achieve single cell resolution of T cell activation and differentiation. To examine these data we first used Uniform Manifold Approximation

and Projection (UMAP (34)) to visualise the phenotypic diversity of T cells at each time-point. Cells close to each other in the UMAP space are phenotypically similar whereas dissimilar cells are far apart. Remarkably, we found that the global structure of the T cell compartment appeared stable between baseline and diagnosis despite the profound loss of lymphocytes from peripheral blood (Figure 3A). On the other hand, a dense population of T cells appeared *de novo* at T6 when lymphocyte counts returned to baseline values (Figure 1B). Inspection of marker expression showed that these were predominantly $CD4^+$ T cells with an effector memory ($CD45RO^+$ $CCR7^-$) and activated ($CD38^{hi}$ $Bcl2^{lo}$) phenotype (Figure 3B and Supplemental Figure 1). The latter marker combination revealed that *P. vivax* could activate up to one quarter of the entire T cell compartment (Figure 3C).

To comprehensively describe these phenotypic changes we used FlowSOM clustering (35) to assign each T cell to one of 34 unique clusters and then tracked the frequency of each cluster through time (Supplemental Figures 2 and 3). To identify differentially abundant clusters at each time-point (relative to baseline) we performed linear regression on cell count data using edgeR (36, 37). We found no clusters were differentially abundant at C10 (FDR < 0.05 and absolute fold-change > 2) and only one cluster at diagnosis (a decrease in $CD161^+$ gamma delta T cells). That only one of 34 clusters significantly changed in their relative size as the host became lymphopenic indicates that T cells are proportionally pulled out of circulation regardless of lineage or function. Using the same significance cut-offs we identified nine clusters that increased in abundance at T6, comprising five $CD4^+$ and two $CD8^+$ T cell subsets plus one MAIT and one gamma delta subset (Figure 4A-B). Crucially, all displayed a $CD38^{hi}$ $Bcl2^{lo}$ phenotype (Figures 3B and 4A).

We then used a complementary method of analysis to examine differential marker expression through time, which can identify early activation events and phenotypic changes in cell subsets that may not increase in abundance (Supplemental Figure 4). This analysis revealed only very minor changes in circulating T cells at the peak of infection - a small increase in expression of CD38 on naive $CD4^+$ T cells and the upregulation of T-bet in $CD8^+$ TEMRA and gamma delta T cells. In contrast, there were major phenotypic changes at T6 with the majority of differentially expressed markers (including death receptors and cytotoxic molecules) found on $CD4^+$ and $CD8^+$ T cells with a memory phenotype. Surprisingly, only two markers (Foxp3 and CTLA4) were differentially expressed on Tregs at T6 and none at diagnosis, which emphasises the absence of overt regulatory pathways operating in peripheral blood. All together, these results suggest that innate-like and adaptive T cells are indiscriminately recruited out of the circulation and activated by *P. vivax*. The breadth and scale of T cell activation considerably exceeds what has been observed in other human challenge models, including typhoidal *Salmonella* (38) and influenza A (39).

Activated T cells are functionally heterogeneous

To elucidate the function of activated T cells as they re-enter the circulation we inspected the median expression values of proliferation and differentiation markers in the nine clusters that increased in abundance at T6 (Figure 5A and Supplemental Figure 5). And because we found more than half of all activated T cells were $CD4^+$ (with five distinct clusters contained within this lineage (Figure 5B)) we focussed on the heterogeneity of this adaptive response. High CD38 and low Bcl2 expression were shared features of all significant $CD4^+$ clusters and 4/5 displayed an effector memory phenotype ($CD45RO^+$ $CCR7^-$). The one exception was a small cluster of activated central memory-like cells ($CD45RO^+$ $CCR7^+$). By summing these five $CD45RO^+$ clusters we found that *P. vivax* activated 20-35% of non-naive $CD4^+$ T cells and the largest cluster had a $CD27^-$ cytotoxic phenotype (perforin$^+$ granzyme B^+) (Figure 5A-C).

HLA-DR and ICOS were frequently upregulated on activated $CD4^+$ T cells and we found widespread expression of inhibitory receptors, such as PD1 and CTLA4 (Figure 5D). These checkpoint inhibitors have been used as shorthand for exhaustion and yet the majority of activated clusters were $CD28^{hi}$, T-bet$^+$ and proliferative (Ki-67^+). Our data therefore suggested that these cells were functional and polarised towards an inflammatory T_H1 fate (Figure 5A). To specifically test for exhaustion or anergy at T6 we stimulated whole blood with PMA/Ionomycin and quantified cytokine production *ex vivo* (Supplemental Figure 6). Activated $CD38^{hi}$ T cells were polyfunctional and retained their capacity to produce all of the hallmark cytokines associated with T_H1, T_H2, T_H17 and T_{FH} differentiation. *P. vivax* does not therefore exhaust activated $CD4^+$ T cells, which can respond to mitogenic stimulation at least as well as resting ($CD38^{lo}$) cells. In summary, $CD4^+$ T cells with an effector memory phenotype dominate the response to *P. vivax* and display marked heterogeneity in their expression of key functional markers. These data therefore emphasise the complexity of $CD4^+$ T cell activation and differentiation in vivax malaria.

T cell activation is independent of systemic inflammation

Innate-like and adaptive T cells have distinct ligand requirements for TCR signaling and yet every major T cell lineage was activated by *P. vivax* (Figure 4 and Supplemental Figure 4). We therefore hypothesised that the scale and breadth of the T cell response may indicate bystander (antigen-independent) activation, which can be caused by systemic inflammation (40, 41). To investigate the relationship between interferon-stimulated inflammation and T cell activation we constructed a Pearson correlation matrix (Figure 6A). We input the log2 fold-change of each plasma analyte with an FDR < 0.05 and the log2 fold-change of each activated T cell cluster (defined as $CD38^{hi}$ $Bcl2^{lo}$). Fold-change was calculated for each feature at

either diagnosis or T6 (relative to baseline) depending on when the peak response was observed. Hierarchical clustering revealed extensive positive correlation between inflammatory cytokines, chemokines and coagulation. In contrast, only one T cell cluster correlated highly with these analytes ($r > 0.8$ for activated $CD8^+$ effector memory) and just two clusters showed weak correlations (activated $CD161^+$ gamma delta and activated $CD4^+$ effector memory). Instead, the majority of T cell clusters (8/11) were placed into a separate clade together with ALT, which indicates that the majority of the T cell response is co-regulated but operates independently of systemic inflammation.

We next looked in detail at the relationship between T cell activation and ALT. Elevations in circulating ALT were positively correlated with the expansion of four activated $CD4^+$ T cell clusters (including cytotoxic effector memory cells) as well as activated Tregs ($r = 0.97$). Because this analysis was looking for independent relationships with each cluster we decided to repeat this analysis at a subset level. To this end, we calculated the correlation between lineage-specific T cell activation and absolute levels of ALT (Figure 6B). We found ALT was strongly associated with activated $CD4^+$ T cells ($r = 0.791$) and regulatory T cells ($r = 0.816$) but not innate-like MAIT ($r = 0.147$) or gamma delta T cells ($r = 0.107$). These data therefore reveal no clear relationship between the intensity of systemic inflammation at diagnosis and the magnitude of the T cell response at T6. Instead, they indicate that $CD4^+$ T cell activation may accurately predict collateral tissue damage and injury.

Parasite species regulates T cell activation and differentiation

Last of all, we performed direct comparative analyses to ask whether the immune response to *P. vivax* differed from that to *P. falciparum*. Thirteen malaria-naive volunteers were infected with *P. falciparum* (clone 3D7) by direct blood challenge during the VAC063 (42) and VAC063C (43) CHMI trials; crucially, diagnosis and treatment thresholds were analogous to VAC069A (*P. vivax*) and circulating parasite densities were comparable at the peak of infection (Figure 7A and Supplemental Figure 7). What's more, the magnitude and kinetics of lymphopenia were equivalent between parasite species (Figure 7B). Initially, we compared transcriptional signatures in whole blood using time-matched samples. Differentially expressed genes were identified at diagnosis and T6 (relative to baseline) in both volunteer cohorts using DESeq2 (adj $p < 0.05$ and absolute fold-change > 1.5). The DEG from each cohort were then combined at each time-point to identify significantly enriched GO terms and functional network analysis was performed using ClueGO. Importantly, information was retained to indicate what fraction of associated genes for each GO term derived from *P. vivax* or *P. falciparum* infected volunteers.

At diagnosis we found 289 GO terms of which 282 (97.58%) were shared between cohorts (Figure 7C). These shared GO terms organised into functional groups that related to host defence and cytokine production (Figure 7D). Remarkably, we found

only 7 GO terms (2.42%) with associated genes that majoritively derived from one volunteer cohort. All of these cohort-specific GO terms were located in the same region of the ClueGO network and were enriched in volunteers infected with *P. vivax* - this response was characterised by downregulation of structural ribosomal gene expression, which can be induced by type I interferon signaling (44). In contrast to diagnosis, only 151/235 (64.3%) GO terms were shared at T6 and these features related to cell cycle progression (Figure 7E-F). All of the remaining GO terms (84/235 or 35.7%) were predominantly derived from just one dataset (*P. falciparum*) and these terms were accessory to cell division, such as DNA replication. These data therefore suggest that *P. vivax* may trigger increased interferon signaling at the peak of infection but *P. falciparum* drives a much stronger proliferative response, which is observed when lymphocytes return to the circulation after parasite clearance.

To explore these possibilities we compared the acute phase response to *P. vivax* and *P. falciparum* using a bead-based protein assay and the $CD4^+$ T cell response by CyTOF. First, we used mixed effects models to quantify differences in systemic inflammation and coagulation at diagnosis and T6. We found a significant increase in IFNγ and the interferon-responsive chemokine CXCL9 in volunteers infected with *P. vivax* (Figure 8A). Surprisingly, none of the 39 plasma analytes were significantly higher in volunteers infected with *P. falciparum* at either time-point. In contrast, CyTOF revealed that *P. falciparum* drives increased activation of $CD4^+$ and regulatory T cells (Figure 8B-C). This adaptive response was so pronounced that a clear transcriptional signature of T_H1 polarisation could be detected in whole blood in volunteers infected with *P. falciparum* (but not *P. vivax*) (Figure 8D). All together, these data demonstrate that *P. vivax* can induce higher levels of systemic inflammation but *P. falciparum* promotes increased $CD4^+$ T cell activation and terminal differentiation.

Discussion

High dimensional protein and RNA-sequencing data show that *P. vivax* can induce an enhanced interferon-stimulated response (cf *P. falciparum*) in a naive human host, which likely explains its reduced pyrogenic threshold. Indeed, we have recorded fever in 17/19 (*P. vivax*) versus 23/39 (*P. falciparum*) volunteers in all of our blood-stage CHMI studies (89.5% versus 59.0%, p = 0.0168 by Barnard's unconditional exact test (includes unpublished trials)). This is unlikely to be explained by the increased time taken to reach the treatment threshold with *P. vivax* (Supplemental Figure 7) because there is no measurable transcriptional response prior to patency (as shown in this study and others (24)). Instead, we suggest that this is a consequence of more sensitive pathogen sensing by innate immune sentinels. In small animal models, malaria parasites are first detected in the bone marrow by plasmacytoid dendritic cells, which produce type I interferon to trigger emergency myelopoiesis and the release of activated monocytes and neutrophils (45, 46). This model is well supported by transcriptional evidence of interferon signaling in the bone marrow of macaques infected with *P. cynomolgi* (47) and the accumulation of myeloid cells with an interferon-stimulated gene signature in the circulation of *P. vivax* infected patients (17, 18). The transcriptional changes we observe at diagnosis are therefore likely to represent the trafficking of activated monocytes and neutrophils from bone marrow to blood. So why would this innate response differ between *P. vivax* and *P. falciparum*? Perhaps *P. vivax* accumulates in higher numbers within the bone marrow parenchyma (4) increasing the availability of parasites for uptake by immune sentinels. Together with the increased abundance of CpG motifs in the *P. vivax* genome (15, 16) this may enhance TLR9 signaling and in turn amplify the production of type I interferon. Sampling of bone marrow in future CHMI studies will allow us to directly test this hypothesis *in vivo*.

A key function of interferon-stimulated inflammation is the release of chemotactic factors that recruit T cells out of the circulation and into inflamed tissues, including the spleen. We found a significant increase in plasma CXCL9 and CXCL10 at the peak of infection, which coincided with profound lymphopenia. The surface-bound receptor for these chemokines is CXCR3, which is a hallmark of T_H1 polarised memory $CD4^+$ T cells and cytotoxic effector $CD8^+$ T cells (48). As such, we expected that these T cell subsets would preferentially be recruited out of the circulation and were surprised to find that the relative abundance of every T cell cluster was essentially unchanged at diagnosis. Our data therefore reveal an indiscriminate mechanism of recruitment that pulls all T cells (regardless of lineage or function) out of peripheral blood. Furthermore, it was surprising that we found almost no evidence of T cell activation at diagnosis (either by cluster abundance or differential marker expression). Evidently, activated T cells do not commonly recirculate during infection and this has major implications for human studies that analyse adaptive responses prior to drug treatment. In the absence of direct access to tissue samples T cell

function should be assessed after their release back into the circulation, which occurs six days after parasite clearance. At this time-point we find that up to one quarter of the entire T cell compartment is activated, including half of all gamma delta T cells. How does infection trigger such widespread activation? This is unlikely to be a direct xenobiotic effect of anti-malarial drugs as artemisinin and its derivatives have been shown to inhibit T cell responses in a dose-dependent manner *in vitro* and *in vivo* (49, 50). Instead, an important clue might derive from the activation of MAIT cells, which recognise riboflavin-derived antigens presented on an MHC-like molecule (51). Malaria parasites can not synthesise riboflavin, which suggests that MAIT cells are not responding in an antigen-specific manner but acting as sensors of tissue inflammation (they can be activated directly by IL-12 and IL-18 (41)). Adaptive T cells can also be activated via this route (40) raising the intriguing possibility that *P. vivax* may cause bystander activation of human T cells. In support of this idea, TCRβ sequencing in mice infected with *P. chabaudi* has revealed polyclonal activation of $CD4^+$ T cells within the inflamed spleen (52).

Activated $CD4^+$ T cells account for more than half of the T cell response to *P. vivax* and all have a memory ($CD45RO^+$) phenotype. This may indicate that $CD4^+$ T cells specific for irrelevant pathogens (or vaccine epitopes) are activated and that we are observing the clonal expansion of pre-existing memory cells. Compared to naive T cells, memory cells are more easily activated in the absence of TCR signals (40, 53). Alternatively, these may not be *bona fide* memory cells but instead short-lived effectors that are specific for a large and diverse pool of *Plasmodium* epitopes. Future studies should therefore prioritise investigating the antigen specificity and clonality of activated cells; this is particularly important because effector and regulatory T cells activated via TCR signals may be functionally distinct from those activated through bystander mechanisms. In the meantime, our data show that the dominant $CD4^+$ T cell cluster displayed a terminally differentiated $CD27^-$ cytotoxic phenotype; cells pushed down this route of differentiation typically arise in the context of chronic stimulation or autoinflammatory disease (54-56). These results therefore highlight the potency of activating signals within inflamed tissues and the potential pathogenicity of the T cell response to *P. vivax*.

Nevertheless, our data do not support a model of infection-induced exhaustion. Most of the $CD38^{hi}$ T cell clusters upregulated inhibitory receptors *in vivo* and yet retained their capacity to respond vigorously to mitogenic stimulation and produce functionally diverse cytokines *ex vivo*. Similar observations have been made in *P. vivax* infected patients (57). It remains possible that features of exhaustion may manifest during chronic infection but at present there is little evidence to support T cell dysfunction in acute disease. Similarly, there is little evidence that regulatory T cells suppress effector responses early in infection. Tregs obtained from *P. vivax* infected patients have a reduced capacity to control $CD4^+$ T cell proliferation and IFNγ production in suppressor assays (58) and in our study the abundance of activated Tregs did not significantly increase at diagnosis or T6. Functional Tregs may operate within

inflamed tissues (and this should be assessed after their return to the circulation) but it seems likely that regulatory networks are simply overwhelmed by the T_H1 polarised effector response (as observed for *Toxoplasma gondii* (59)).

So what are the likely consequences of this aggressive T cell response for the course and outcome of infection? The production of class-switched IgG antibodies specific for the merozoite protein $MSP1_{19}$ indicates functional B cell help in our study (26). Unfortunately, we have not yet been able to examine the frequency or function of circulating T_{FH} cells at T6. Nonetheless, circulating $CD4^+$ T cells with a T_{FH} phenotype have been reported in patients infected with *P. vivax* and this coincided with an increase in plasma IL-21 (60), which was significantly upregulated in our volunteers. Whether these antibodies can effectively neutralise infected reticulocytes *in vivo* could be assessed by reinfecting volunteers. The direct cytolysis of infected reticulocytes by activated cytotoxic $CD8^+$ T cells also requires validation *in vivo*. What does seem clear, however, is that the adaptive T cell response correlates closely with collateral tissue damage. Liver injury is a common feature of clinical and experimental malaria and occurs independently of the drug used or treatment regime (61, 62). It has been suggested that systemic inflammation might trigger hepatocyte death but our data do not support this hypothesis; we find no relationship between cytokine/chemokine levels and raised ALT. Instead, we propose that T cell trafficking to the liver (which is commonly observed during the resolution of an immune response and facilitates the clearance of apoptotic T cells (63)) may lead to off-target cytotoxicity. In agreement, raised ALT in macaques infected with *P. cynomolgi* coincides with inflammatory infiltrates (inc. lymphocytes) in the liver (64).

Remarkably, CyTOF and RNA-sequencing data show that *P. falciparum* causes increased activation and polarisation of $CD4^+$ T cells (cf *P. vivax*). How do we reconcile increased T cell activation with lower systemic inflammation? Parasitaemia was comparable between volunteer cohorts but it remains possible that the total pathogen load was higher for *P. falciparum* because of increased accumulation in inflamed tissues. An alternative explanation is that *P. falciparum* encodes more immunogenic proteins that can cross-react with pre-existing memory T cells. In any case, more T cell activation may be one of the reasons why *P. falciparum* more frequently causes severe disease. As infection progresses, an excess of activated T cells could exacerbate inflammation, coagulation and collateral damage to promote endothelium activation and sequestration in their tissue environment. In this context, it is important to note that the pathogenicity of T cells in infants and children has not yet been adequately assessed after their return to the circulation (65). And furthermore, the disconnect between systemic inflammation and tissue-specific responses might explain why field studies consistently fail to find reproducible associations between circulating protein markers of inflammation and disease severity.

Could increased T cell activation also explain why clinical immunity takes far longer to develop against *P. falciparum*? After all, this may lead to increased exhaustion if

infection is not curtailed by drug treatment. Clinical immunity requires emergency myelopoiesis to be disarmed within the bone marrow to prevent the release of activated monocytes and neutrophils (and pyrogenic cytokines). Immune sentinels therefore need to tolerate malaria parasites (or become refractory to interferon signaling) and this adaptation may require T cell help (45). Alternatively, clinical immunity might be promoted by infection-induced remodeling of the bone marrow or reprogramming of innate immune progenitors (66). In this scenario, the accumulation of *P. vivax* in the bone marrow parenchyma might have an associated cost (a reduced pyrogenic threshold) but the benefit of faster clinical immunity. Developing human challenge models that incorporate reinfection and tissue sampling would allow us to ask how parasite biology shapes the discrete patterns of disease observed in human malaria.

Limitations of the study

We measure shared (or common) responses to *P. vivax* at a group-level and can't quantify the heterogeneity between volunteers, which is likely to be a critical determinant of infection outcome. Indeed, our plasma data suggest that v07 does not trigger a detectable inflammatory response at diagnosis, which is in-line with our observation of immune quiescence in one third of volunteers undergoing CHMI with *P. falciparum* (67). On the other hand, we find that every volunteer triggers widespread activation of innate-like and adaptive T cells (including v07), and terminally differentiated $CD27^-$ cytotoxic $CD4^+$ T cells are a conserved feature across the cohort. Our results therefore emphasise the disconnect between systemic inflammation and T cell activation in human malaria. Nonetheless, future studies should increase sample size so that the host response can be mapped through time in each individual to identify unusual outcomes. Human T cells are inherently plastic (68) and a larger sample size is likely to reveal further diversity and identify rare T cell phenotypes that might be critical for pathogenesis. In the meantime, caution should be taken not to generalise these findings to every individual infected with *P. vivax*. A second important caveat is that infections were terminated at a parasite density much lower than would be observed in endemic settings. The impact of increasing pathogen load on T cell activation (or exhaustion) is difficult to predict and we are not aware of any post-treatment data from patients infected with *P. vivax* or *P. falciparum*. This is a critical knowledge gap that urgently needs to be addressed. What's more, the pathogen load within lymphoid tissues (such as bone marrow or spleen) might be a more important determinant of the host response than the number of circulating parasites but at present it is not possible to quantify this. Direct tissue access (via fine needle aspiration (69)) would overcome this limitation and reveal the biology of T cell activation where it matters most.

Methods

Note that additional details regarding methodology and statistical analysis can be found online in the Supplemental Methods.

VAC069A clinical trial

Six volunteers were recruited to test the infectivity of a new cryopreserved stabilate containing a clonal field isolate of *P. vivax* (PvW1); this stabilate had carefully been prepared for use in CHMI by blood challenge. The CHMI trial was named VAC069A and is reported in full in reference (26). In brief, cryopreserved vials of stabilate were thawed, washed and diluted under aseptic conditions, and then administered to healthy malaria-naive adult volunteers by intravenous injection. Volunteers each received an inoculum containing between 116 and 2232 PvW1 genome copies; variation in the infectious dose had no measurable effect on parasite multiplication rate (26) and does not influence the severity or outcome of human malaria (70). After inoculation whole blood was drawn twice daily to determine circulating parasite density by qPCR (target gene = 18S ribosomal RNA); thick blood smears were also evaluated by experienced microscopists at each time-point. Treatment was initiated once two diagnostic conditions were fulfilled: more than 5,000 or 10,000 parasite genome copies ml^{-1}, positive thick blood smear and/or symptoms consistent with malaria. Treatment usually consisted of artemether and lumefantrine (Riamet) or atovaquone and proguanil (Malarone) if Riamet was contraindicated. Volunteer 05 received Malarone, all other volunteers received Riamet.

All reported clinical symptoms (arthralgia, back pain, chills, diarrhoea, fatigue, fever, headache, malaise, myalgia, nausea, pyrexia, rigor, sweating and vomiting) were recorded as adverse events and assigned a severity score: 1 - transient or mild discomfort (no medical intervention required); 2 - mild to moderate limitation in activity (no or minimal medical intervention required); 3 - marked or severe limitation in activity requiring assistance (may require medical intervention). At baseline, C7, C14 (if undiagnosed), diagnosis, T1 and T6 full blood counts and blood chemistry were evaluated at the Churchill and John Radcliffe hospitals in Oxford, providing 5-part differential white cell counts and quantification of electrolytes, urea, creatinine, bilirubin, alanine aminotransferase (ALT), alkaline phosphatase (ALP) and albumin. Blood for immunological analyses was collected in EDTA tubes by venepuncture at the indicated time-points, and samples were processed immediately for downstream applications in a laboratory adjacent to the clinical facility.

CyTOF sample acquisition

Whole blood samples were taken at baseline, C10, diagnosis and T6 and stabilised in whole blood preservation buffer (Cytodelics AB) within 30 minutes of blood draw. Preserved samples were stored at -80°C. Samples were thawed in a water bath at 37°C and then fixed and red cell lysed using the whole blood preservation kit

(Cytodelics AB). Fixed samples were washed, permeabilised and barcoded using the cell-ID 20-plex Pd barcoding kit (Fluidigm). Barcoded samples were then pooled and counted before resuspending in cell staining buffer (Fluidigm) at 40 x 10^6 cells ml^{-1}. An equal volume of freshly prepared antibody cocktail (Supplemental File 2) was added for 30 minutes at room temperature under gentle agitation. After washing, samples were resuspended in nuclear antigen staining buffer (Fluidigm) for 30 minutes at room temperature. Samples were then washed in nuclear antigen staining perm buffer (Fluidigm) and antibodies for intracellular/nuclear targets were added for a further 45 minutes. After another round of washing the cells were fixed with 1.6% paraformaldehyde in PBS for 10 minutes and finally resuspended in fix and perm buffer plus 72.5nM cell-ID 191Ir/193Ir intercalator (both Fluidigm) at a concentration of 2 x10^6 cells ml^{-1}. Cells were incubated overnight at 4°C. Sample acquisition was performed on a freshly tuned Helios mass cytometer using the WB injector and acquired with 10% normalisation beads (140Ce, 151Eu, 165Ho and 175Lu, all Fluidigm). Both staining and sample acquisition were carried out in two batches (all time-points for 3 volunteers per batch). On each acquisition day, pooled cells were counted again before removing an aliquot of 2 x 10^6 cells; aliquots were washed twice in cell staining buffer and resuspended in 1ml cell acquisition solution (Fluidigm). Each aliquot was acquired completely before washing and processing the next aliquot until all pooled samples had been acquired. Cells were acquired at a rate of 300-500 events per second.

CyTOF data processing

FCS files were generated using CyTOF software (v6.7) followed by normalisation (71) and debarcoding (72) using the CATALYST workflow described in (73). Single-stained beads were used for compensation (using non-negative linear least squares regression (74)) and FCS files were gated in the Cytobank web portal (Beckman Coulter) to exclude normalisation beads and doublets. Singlet T cells ($CD45^+$ $CD3^+$) were taken forward for analysis. Intensity distributions of each channel were inspected to remove channels of low variance (CD14, Tim3, Integrin β7, CD56, CD16, CD49d, CD103, CXCR5). Of note, low variance in these channels does not necessarily reflect uniform or absent expression of these markers; it could also be due to inefficient staining of fixed samples with these antibody clones. The remaining 28 markers were used for both UMAP projections and FlowSOM clustering.

UMAP (34) creates low-dimensional projections of high-dimensional data. Here cells were grouped according to marker expression intensity and embedded in a 2D plane such that phenotypic similarity within and between populations is preserved in the Euclidean distance of the projection. We used its R implementation in the scater package (75), which in turn relies on uwot (github.com/jlmelville/uwot). Features were scaled to unit variance and the 15 nearest neighbours were considered for embedding. UMAP coordinates were then exported for visualisation using ggplot2 (76).

FlowSOM (35) uses self-organising maps to efficiently categorise cytometry data into non-overlapping cell populations. Clustering was performed with a target cluster number of 100 and metaclustering with a target number of 45. This approach purposefully overclustered the data to resolve potentially small subsets, a trade-off that can split phenotypically similar cells into more than one population (77). Overclustering was addressed by manual inspection and merging of phenotypically similar populations; in this way, each T cell was classified into one of 34 unique clusters. Names were assigned manually using activation, lineage and memory markers to broadly categorise each T cell cluster; when more than one cluster was placed into the same category clusters were given an accessory label to highlight their unique phenotype or property (e.g. skin-homing, indicated by the expression of CLA). The ComplexHeatmap package (78) was used to visualise T cell cluster phenotypes; the arcsine transformed signal intensity of each marker was independently scaled using a 0-1 transformation across all 34 clusters.

CyTOF data analysis

For differential abundance analysis of T cell clusters we followed the workflow laid out in (73). FlowSOM cluster cell counts were modelled linearly with time-point as a dependent categorical variable and volunteer as a fixed effect using the diffcyt (37) implementation of edgeR (36). The edgeR functions automatically normalise cluster counts for the total number of cells and improve statistical power by sharing information on cluster count variance between clusters. Using moderated f-tests, pairwise comparisons were performed relative to baseline and clusters with an FDR < 0.05 and absolute fold-change > 2 were deemed to vary significantly through time. We also assessed whether marker expression varied significantly through time. To do this we merged clusters of the same lineage according to their expression of CD4, CD8α, Vδ2 and Vα7.2. $CD4^+$ and $CD8^+$ T cells were then split into naive, effector, effector memory, central memory and TEMRA subsets based on their expression of the markers CD45RA, CD45RO, CD57 and CCR7. All regulatory T cells ($CD25^{hi}$ $CD127^{neg}$) were merged into a single cluster as were all double negative, gamma delta and MAIT cells. Linear regression models were fit using limma (which is optimised for continuous data) incorporating time-point, volunteer and acquisition batch as covariates. To independently assess differential marker expression (relative to baseline) moderated t-tests were used to test regression coefficients; a shift in median expression of at least 10% and an FDR < 0.05 were required for significance. Results were visualised using ComplexHeatmap with row-wise z-score transformed marker intensities shown for each subset.

Comparison to *P. falciparum*

To compare the immune response induced by *P. vivax* versus *P. falciparum* we used data from two previously conducted CHMI trials (VAC063 and VAC063C); the VAC063 trial is described in full in reference (42) and the VAC063C trial is reported

in (43). In brief, thirteen malaria-naive adult volunteers (ten in VAC063 and three in VAC063C) were inoculated with *P. falciparum* (clone 3D7) by intravenous injection of infected red cells (452-857 parasites per volunteer). The inoculum derived from a cryopreserved stabilate that was thawed, washed and diluted under aseptic conditions immediately before challenge. Starting one day after infection volunteers attended clinic for assessment and blood sampling every 12-hours, and circulating parasite density was measured in real time by qPCR (target gene = 18S ribosomal RNA). At diagnosis (symptomatic with more than 5,000 parasites ml^{-1} or asymptomatic above 10,000 parasites ml^{-1}) volunteers were treated with either Riamet or Malarone (if Riamet was contraindicated). Blood for immunological analyses was collected in EDTA tubes by venepuncture at baseline, diagnosis, T6 and C90 (memory time-point). To analyse T cell activation, whole blood samples were preserved during VAC063C and processed for CyTOF exactly as described for *P. vivax*. Data processing was also performed analogously to VAC069A and FlowSOM was used to place each T cell into a phenotypically unique cluster. Note that clustering was performed independently on the VAC069A and VAC063C datasets. For each volunteer, the proportion of activated $CD4^+$ T cells and regulatory T cells was then calculated by summing the frequency of all clusters with a $CD38^{hi}$ $Bcl2^{lo}$ phenotype. To compare parasite species specific differences in T cell activation we used Wilcoxon rank sum exact test (two-tailed).

Statistics

Analysis was carried out in R (v3.6.3) unless otherwise stated.

Multiplexed plasma analysis: protein concentrations were log10 transformed and linear regression models were fit separately for each analyte. For the *P. vivax* dataset, linear regression models were fit including time-point and volunteer identity as fixed effects using the R package stats. To compare *P. vivax* and *P. falciparum*-infected volunteers, mixed effects models were fit including time-point and parasite species as fixed effects and volunteer identity as a random effect using lme4. Linear hypothesis testing was then performed using multcomp. For analysis of *P. vivax*, t-tests were used to test the significance of model coefficients (each time-point versus baseline). Similarly, to compare *P. vivax* versus *P. falciparum* we used z-tests. P values were adjusted for multiple testing using Benjamini-Hochberg correction and an FDR < 0.05 was considered significant.

Whole blood RNA-sequencing: DESeq2 (29) was used to identify DEG at each time-point (cf baseline) and adjusted p values were obtained using Wald tests (incorporating time-point and volunteer identity as covariates). Analysis was performed independently on the *P. vivax* and *P. falciparum* datasets. In both cases, DEG were classified as those with an absolute fold-change > 1.5 and an FDR < 0.05. Genes with multiple differentially expressed transcripts were filtered to retain the transcript with the lowest adjusted p value. GO analysis was carried out in Cytoscape (version 3.8.0) using the ClueGO plugin (version 2.5.7) (30, 31) and

networks were constructed by combining the lists of differentially expressed genes from volunteers infected with *P. vivax* and *P. falciparum*. Importantly, for every GO term information on what fraction of associated genes was derived from each list was retained. Any GO term containing > 65% associated genes from a single volunteer cohort was considered to be enriched in that infection model, otherwise GO terms were considered to be shared.

Pearson correlation; the fold-change of each T cell cluster and plasma analyte was calculated using raw cluster percentages or plasma concentrations, respectively. For each feature, these were calculated at diagnosis or T6 (relative to baseline) according to their largest absolute fold-change. All data were log2 transformed and Pearson correlation was performed using the cor function from the stats package. Correlation coefficients were then used for hierarchical clustering by Euclidean distance using ComplexHeatmap.

Study approval

The VAC069A, VAC063 and VAC063C CHMI trials were sponsored by the University of Oxford and received ethical approval from the UK NHS Research Ethics Service - VAC069A (South Central Hampshire A, reference 18/SC/0577), VAC063 (Oxfordshire Research Ethics Committee A, reference 16/SC/0345) and VAC063C (South Central Oxford A, reference 18/SC/0521). All trials were registered on ClinicalTrials.gov (NCT03797989, NCT02927145 and NCT03906474, respectively) and were conducted in the UK at the Centre for Vaccinology and Tropical Medicine (University of Oxford). Trials were conducted according to the principles of the current revision of the Declaration of Helsinki 2008 and in full conformity with the ICH Guidelines for Good Clinical Practice. Volunteers signed written consent forms and consent was checked prior to each CHMI.

Data availability

RNA-sequencing data from VAC069A have been deposited in the European Genome-phenome Archive (EGA) and are accessible through accession number EGAS00001003847. Sequencing data from VAC063/VAC063C have been deposited in NCBI's Gene Expression Omnibus and are accessible through accession number GSE172450. CyTOF data are available at flowrepository.org and can be accessed through experiment numbers FR-FCM-Z3HA (VAC069A) and FR-FCM-Z47Z (VAC063C).

Author contributions

FAB and PJS designed the research study; FAB, DMS, MM, ACH and NJE conducted experiments; FAB, DMS, MM, YT, TAR, ACH and NJE acquired data; FAB, DMS, ACH, AI, GN and PJS analysed the data; YT, TAR, SES, JRB, AMM and SJD provided reagents; AK, JCR, AMM, SJD and PJS provided project management

and oversight; FAB and PJS wrote the manuscript; all authors edited and approved the final manuscript.

Acknowledgements

The VAC069A trial was supported in part by funding from the European Union's Horizon 2020 Research and Innovation programme under grant agreement for MultiViVax (number 733073). The VAC063 and VAC063C trials were supported in part by the Office of Infectious Diseases, Bureau for Global Health, U.S. Agency for International Development (USAID) under the terms of the Malaria Vaccine Development Program (MVDP) contract AID-OAA-C-15-00071, for which Leidos, Inc. is the prime contractor. The opinions expressed herein are those of the authors and do not necessarily reflect the views of the USAID. All clinical studies were further supported by the National Institute for Health Research (NIHR) Oxford Biomedical Research Centre (BRC). The views expressed are those of the authors and not necessarily those of the NIHR or the Department of Health and Social Care. The authors would like to thank Mandy Sanders and the DNA pipelines team at the Wellcome Sanger Institute for their support with RNA-seq library preparation and data production in VAC069A. RNA-seq libraries for VAC063/VAC063C were prepared and sequenced by Edinburgh Genomics, which is supported through core grants from NERC (R8/H10/56), MRC UK (MR/K001744/1) and BBSRC (BB/J004243/1). CyTOF data were generated in the mass cytometry facility at the Weatherall Institute of Molecular Medicine (University of Oxford), which is supported by MRC Human Immunology Unit core funding (MC_UU_00008) and the Oxford Single Cell Biology Consortium (OSCBC). FAB is the recipient of a Wellcome Trust PhD studentship (grant no. 203764/Z/16/Z). JCR and the DNA pipelines team (Sanger) are supported by funding from the Wellcome Trust (grant no. 206194/Z/17/Z); JCR is also a Wellcome Investigator (grant number 222323/Z/21/Z). SJD is a Jenner Investigator, the recipient of a Wellcome Trust Senior Fellowship (grant no. 106917/Z/15/Z) and a Lister Institute Research Prize Fellow. And PJS is the recipient of a Sir Henry Dale Fellowship jointly funded by the Wellcome Trust and the Royal Society (grant no. 107668/Z/15/Z). We would like to extend our thanks to the VAC069A, VAC063 and VAC063C clinical and laboratory study teams for assistance, and all of the volunteers who participated in these trials.

References

1. Battle KE, et al. Mapping the global endemicity and clinical burden of Plasmodium vivax, 2000-17: a spatial and temporal modelling study. *Lancet.* 2019;394(10195):332-43.
2. Thriemer K, et al. The risk of adverse clinical outcomes following treatment of Plasmodium vivax malaria with and without primaquine in Papua, Indonesia. *PLoS Negl Trop Dis.* 2020;14(11):e0008838.
3. Kho S, et al. Hidden Biomass of Intact Malaria Parasites in the Human Spleen. *N Engl J Med.* 2021;384(21):2067-9.
4. Obaldia N, 3rd, et al. Bone Marrow Is a Major Parasite Reservoir in Plasmodium vivax Infection. *mBio.* 2018;9(3).
5. Rahimi BA, et al. Severe vivax malaria: a systematic review and meta-analysis of clinical studies since 1900. *Malar J.* 2014;13:481.
6. Anstey NM, et al. Lung injury in vivax malaria: pathophysiological evidence for pulmonary vascular sequestration and posttreatment alveolar-capillary inflammation. *J Infect Dis.* 2007;195(4):589-96.
7. Gruszczyk J, et al. Transferrin receptor 1 is a reticulocyte-specific receptor for Plasmodium vivax. *Science.* 2018;359(6371):48-55.
8. Luxemburger C, et al. The epidemiology of severe malaria in an area of low transmission in Thailand. *Trans R Soc Trop Med Hyg.* 1997;91(3):256-62.
9. Boyd MF. A review of studies on immunity to vivax malaria. *J Natl Malar Soc.* 1947;6(1):12-31.
10. Ciuca M, et al. Immunity in malaria. *Transactions of the Royal Society of Tropical Medicine and Hygiene.* 1934;27(6):619-22.
11. Collins WE, et al. A retrospective examination of reinfection of humans with Plasmodium vivax. *Am J Trop Med Hyg.* 2004;70(6):642-4.
12. Lin E, et al. Differential patterns of infection and disease with P. falciparum and P. vivax in young Papua New Guinean children. *PLoS One.* 2010;5(2):e9047.
13. Michon P, et al. The risk of malarial infections and disease in Papua New Guinean children. *Am J Trop Med Hyg.* 2007;76(6):997-1008.
14. Antonelli LR, et al. The immunology of Plasmodium vivax malaria. *Immunol Rev.* 2020;293(1):163-89.
15. Parroche P, et al. Malaria hemozoin is immunologically inert but radically enhances innate responses by presenting malaria DNA to Toll-like receptor 9. *Proc Natl Acad Sci U S A.* 2007;104(6):1919-24.
16. Sharma S, et al. Innate immune recognition of an AT-rich stem-loop DNA motif in the Plasmodium falciparum genome. *Immunity.* 2011;35(2):194-207.
17. Antonelli LR, et al. The CD14+CD16+ inflammatory monocyte subset displays increased mitochondrial activity and effector function during acute Plasmodium vivax malaria. *PLoS Pathog.* 2014;10(9):e1004393.

18. Rocha BC, et al. Type I Interferon Transcriptional Signature in Neutrophils and Low-Density Granulocytes Are Associated with Tissue Damage in Malaria. *Cell Rep.* 2015;13(12):2829-41.
19. Junqueira C, et al. Cytotoxic CD8(+) T cells recognize and kill Plasmodium vivax-infected reticulocytes. *Nat Med.* 2018;24(9):1330-6.
20. Collins KA, et al. A Plasmodium vivax experimental human infection model for evaluating efficacy of interventions. *J Clin Invest.* 2020;130(6):2920-7.
21. Herrera S, et al. Successful sporozoite challenge model in human volunteers with Plasmodium vivax strain derived from human donors. *Am J Trop Med Hyg.* 2009;81(5):740-6.
22. McCarthy JS, et al. Experimentally induced blood-stage Plasmodium vivax infection in healthy volunteers. *J Infect Dis.* 2013;208(10):1688-94.
23. Sharp PM, et al. Ape Origins of Human Malaria. *Annu Rev Microbiol.* 2020;74:39-63.
24. Rojas-Pena ML, et al. Transcription Profiling of Malaria-Naive and Semi-immune Colombian Volunteers in a Plasmodium vivax Sporozoite Challenge. *PLoS Negl Trop Dis.* 2015;9(8):e0003978.
25. Woodberry T, et al. Early Immune Regulatory Changes in a Primary Controlled Human Plasmodium vivax Infection: CD1c(+) Myeloid Dendritic Cell Maturation Arrest, Induction of the Kynurenine Pathway, and Regulatory T Cell Activation. *Infect Immun.* 2017;85(6).
26. Minassian AM, et al. Controlled human malaria infection with a clone of Plasmodium vivax with high-quality genome assembly. *JCI Insight.* 2021;6(23).
27. Dos Santos RO, et al. A First Plasmodium vivax Natural Infection Induces Increased Activity of the Interferon Gamma-Driven Tryptophan Catabolism Pathway. *Front Microbiol.* 2020;11:400.
28. Francischetti IM, et al. Blood coagulation, inflammation, and malaria. *Microcirculation.* 2008;15(2):81-107.
29. Love MI, et al. Moderated estimation of fold change and dispersion for RNA-seq data with DESeq2. *Genome Biol.* 2014;15(12):550.
30. Bindea G, et al. ClueGO: a Cytoscape plug-in to decipher functionally grouped gene ontology and pathway annotation networks. *Bioinformatics.* 2009;25(8):1091-3.
31. Mlecnik B, et al. Functional network pipeline reveals genetic determinants associated with in situ lymphocyte proliferation and survival of cancer patients. *Sci Transl Med.* 2014;6(228):228ra37.
32. Hviid L, et al. Rapid reemergence of T cells into peripheral circulation following treatment of severe and uncomplicated Plasmodium falciparum malaria. *Infect Immun.* 1997;65(10):4090-3.
33. Mandala WL, et al. Characterization of Lymphocyte Subsets in Lymph Node and Spleen Sections in Fatal Pediatric Malaria. *Pathogens.* 2022;11(8).

34. McInnes L, et al. UMAP: Uniform Manifold Approximation and Projection for Dimension Reduction. *arXiv:180203426.* 2020.
35. Van Gassen S, et al. FlowSOM: Using self-organizing maps for visualization and interpretation of cytometry data. *Cytometry A.* 2015;87(7):636-45.
36. Robinson MD, et al. edgeR: a Bioconductor package for differential expression analysis of digital gene expression data. *Bioinformatics.* 2010;26(1):139-40.
37. Weber LM, et al. diffcyt: Differential discovery in high-dimensional cytometry via high-resolution clustering. *Commun Biol.* 2019;2:183.
38. Napolitani G, et al. Clonal analysis of Salmonella-specific effector T cells reveals serovar-specific and cross-reactive T cell responses. *Nat Immunol.* 2018;19(7):742-54.
39. Rahil Z, et al. Landscape of coordinated immune responses to H1N1 challenge in humans. *J Clin Invest.* 2020;130(11):5800-16.
40. Raue HP, et al. Cytokine-mediated programmed proliferation of virus-specific CD8(+) memory T cells. *Immunity.* 2013;38(1):131-9.
41. Ussher JE, et al. CD161++ CD8+ T cells, including the MAIT cell subset, are specifically activated by IL-12+IL-18 in a TCR-independent manner. *Eur J Immunol.* 2014;44(1):195-203.
42. Minassian AM, et al. Reduced blood-stage malaria growth and immune correlates in humans following RH5 vaccination. *Med (N Y).* 2021;2(6):701-19.
43. Salkeld J, et al. Repeat controlled human malaria infection of healthy UK adults with blood-stage Plasmodium falciparum: Safety and parasite growth dynamics. *Front Immunol.* 2022;13:984323.
44. Gupta R, et al. Suppression of ribosomal protein synthesis and protein translation factors by Peg-interferon alpha/ribavirin in HCV patients blood mononuclear cells (PBMC). *J Transl Med.* 2012;10:54.
45. Nahrendorf W, et al. Inducible mechanisms of disease tolerance provide an alternative strategy of acquired immunity to malaria. *Elife.* 2021;10.
46. Spaulding E, et al. STING-Licensed Macrophages Prime Type I IFN Production by Plasmacytoid Dendritic Cells in the Bone Marrow during Severe Plasmodium yoelii Malaria. *PLoS Pathog.* 2016;12(10):e1005975.
47. Tang Y, et al. Integrative analysis associates monocytes with insufficient erythropoiesis during acute Plasmodium cynomolgi malaria in rhesus macaques. *Malar J.* 2017;16(1):384.
48. Groom JR, and Luster AD. CXCR3 ligands: redundant, collaborative and antagonistic functions. *Immunol Cell Biol.* 2011;89(2):207-15.
49. Hou L, and Huang H. Immune suppressive properties of artemisinin family drugs. *Pharmacol Ther.* 2016;166:123-7.
50. Wang JX, et al. Investigation of the immunosuppressive activity of artemether on T-cell activation and proliferation. *Br J Pharmacol.* 2007;150(5):652-61.

51. Kjer-Nielsen L, et al. MR1 presents microbial vitamin B metabolites to MAIT cells. *Nature.* 2012;491(7426):717-23.
52. Smith NL, et al. A Conserved TCRbeta Signature Dominates a Highly Polyclonal T-Cell Expansion During the Acute Phase of a Murine Malaria Infection. *Front Immunol.* 2020;11:587756.
53. Weng NP, et al. IL-15 is a growth factor and an activator of CD8 memory T cells. *Ann N Y Acad Sci.* 2002;975:46-56.
54. Appay V, et al. Characterization of CD4(+) CTLs ex vivo. *J Immunol.* 2002;168(11):5954-8.
55. Fonseka CY, et al. Mixed-effects association of single cells identifies an expanded effector CD4(+) T cell subset in rheumatoid arthritis. *Sci Transl Med.* 2018;10(463).
56. Mattoo H, et al. Clonal expansion of CD4(+) cytotoxic T lymphocytes in patients with IgG4-related disease. *J Allergy Clin Immunol.* 2016;138(3):825-38.
57. Costa PA, et al. Induction of Inhibitory Receptors on T Cells During Plasmodium vivax Malaria Impairs Cytokine Production. *J Infect Dis.* 2015;212(12):1999-2010.
58. Costa PAC, et al. Plasmodium vivax Infection Impairs Regulatory T-Cell Suppressive Function During Acute Malaria. *J Infect Dis.* 2018;218(8):1314-23.
59. Oldenhove G, et al. Decrease of Foxp3+ Treg cell number and acquisition of effector cell phenotype during lethal infection. *Immunity.* 2009;31(5):772-86.
60. Figueiredo MM, et al. T follicular helper cells regulate the activation of B lymphocytes and antibody production during Plasmodium vivax infection. *PLoS Pathog.* 2017;13(7):e1006484.
61. Odedra A, et al. Liver Function Test Abnormalities in Experimental and Clinical Plasmodium vivax Infection. *Am J Trop Med Hyg.* 2020;103(5):1910-7.
62. Reuling IJ, et al. Liver Injury in Uncomplicated Malaria is an Overlooked Phenomenon: An Observational Study. *EBioMedicine.* 2018;36:131-9.
63. Crispe IN, et al. The liver as a site of T-cell apoptosis: graveyard, or killing field? *Immunol Rev.* 2000;174:47-62.
64. C JJ, et al. Case Report: Severe and Complicated Cynomolgi Malaria in a Rhesus Macaque Resulted in Similar Histopathological Changes as Those Seen in Human Malaria. *Am J Trop Med Hyg.* 2017;97(2):548-55.
65. Apte SH, et al. A population of CD4(hi)CD38(hi) T cells correlates with disease severity in patients with acute malaria. *Clin Transl Immunology.* 2020;9(11):e1209.
66. Kaufmann E, et al. BCG Educates Hematopoietic Stem Cells to Generate Protective Innate Immunity against Tuberculosis. *Cell.* 2018;172(1-2):176-90 e19.

67. Milne K, et al. Mapping immune variation and var gene switching in naive hosts infected with Plasmodium falciparum. *Elife.* 2021;10.
68. Sallusto F, et al. Do Memory CD4 T Cells Keep Their Cell-Type Programming: Plasticity versus Fate Commitment? T-Cell Heterogeneity, Plasticity, and Selection in Humans. *Cold Spring Harb Perspect Biol.* 2018;10(3).
69. Noe A, et al. Deep Immune Phenotyping and Single-Cell Transcriptomics Allow Identification of Circulating TRM-Like Cells Which Correlate With Liver-Stage Immunity and Vaccine-Induced Protection From Malaria. *Front Immunol.* 2022;13:795463.
70. Glynn JR, et al. Infecting dose and severity of falciparum malaria. *Trans R Soc Trop Med Hyg.* 1995;89(3):281-3.
71. Finck R, et al. Normalization of mass cytometry data with bead standards. *Cytometry A.* 2013;83(5):483-94.
72. Zunder ER, et al. Palladium-based mass tag cell barcoding with a doublet-filtering scheme and single-cell deconvolution algorithm. *Nat Protoc.* 2015;10(2):316-33.
73. Nowicka M, et al. CyTOF workflow: differential discovery in high-throughput high-dimensional cytometry datasets. *F1000Res.* 2017;6:748.
74. Chevrier S, et al. Compensation of Signal Spillover in Suspension and Imaging Mass Cytometry. *Cell Syst.* 2018;6(5):612-20 e5.
75. McCarthy DJ, et al. Scater: pre-processing, quality control, normalization and visualization of single-cell RNA-seq data in R. *Bioinformatics.* 2017;33(8):1179-86.
76. Wickam H. ggplot2: Elegant Graphics for Data Analysis. *Springer-Verlag New York.* 2016.
77. Saeys Y, et al. Response to Orlova et al. "Science not art: statistically sound methods for identifying subsets in multi-dimensional flow and mass cytometry data sets". *Nat Rev Immunol.* 2017;18(1):78.
78. Gu Z, et al. Complex heatmaps reveal patterns and correlations in multidimensional genomic data. *Bioinformatics.* 2016;32(18):2847-9.

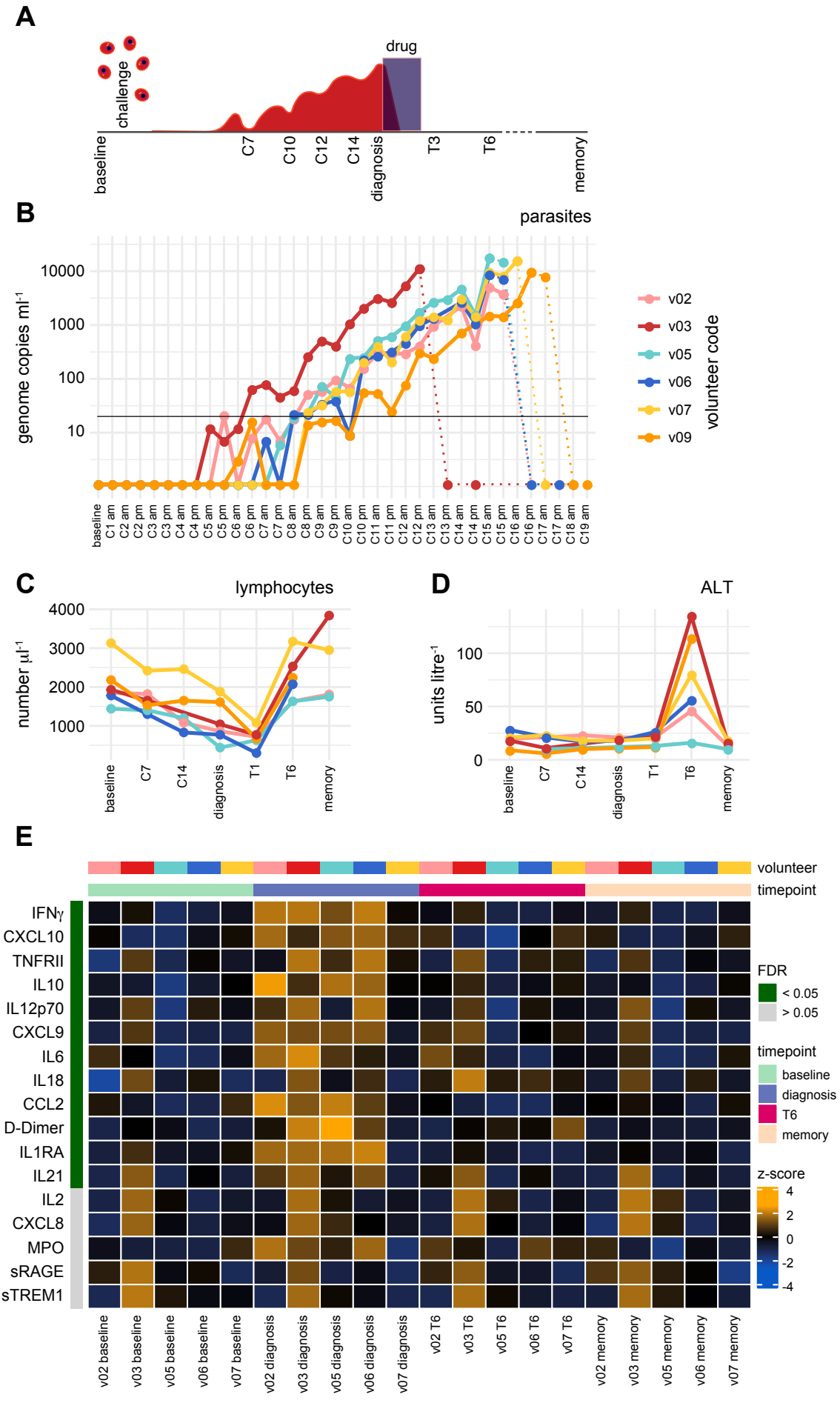
A
drug
challenge
baseline
C7
C10
C12
C14
diagnosis
T3
T6
memory
B
parasites
genome copies ml-1
10000
1000
100
10
v02
v03
v05
v06
v07
v09
volunteer code
C
lymphocytes
number µl-1
4000
3000
2000
1000
D
ALT
units litre-1
100
50
0
E
volunteer
timepoint
IFNγ
CXCL10
TNFRII
IL10
IL12p70
CXCL9
IL6
IL18
CCL2
D-Dimer
IL1RA
IL21
IL2
CXCL8
MPO
sRAGE
sTREM1
FDR
< 0.05
> 0.05
timepoint
baseline
diagnosis
T6
memory
z-score
4
2
0
-2
-4
v02 baseline
v03 baseline
v05 baseline
v06 baseline
v07 baseline
v02 diagnosis
v03 diagnosis
v05 diagnosis
v06 diagnosis
v07 diagnosis
v02 T6
v03 T6
v05 T6
v06 T6
v07 T6
v02 memory
v03 memory
v05 memory
v06 memory
v07 memory

Figure 1. *Plasmodium vivax* triggers interferon-stimulated inflammation. (**A**) Study design and sampling time-points. (**B**) Circulating parasite density was determined twice daily by qPCR. Pre-treatment measurements are shown as solid lines, post-treatment measurements as dotted lines. The limit of quantification (20 genome copies ml^{-1}) is shown by a black line. (**C-D**) Full blood counts and blood chemistry measured (C) lymphocyte frequencies and (D) the concentration of alanine aminotransferase (ALT) throughout infection and convalescence. In (B-D) each line represents one volunteer (n = 6). (**E**) Multiplexed plasma analytes were measured using a custom Legendplex assay. Each row in the heatmap is an analyte and each column a plasma sample. Samples from v09 were excluded after failing QC (n = 5). Linear regression was used to identify analytes that varied across the volunteer cohort at each time-point (compared to baseline) and these are ordered by FDR. An FDR < 0.05 was considered significant after adjusting for multiple testing (Benjamini-Hochberg). Only 17 of the 39 analytes measured are shown (those with the lowest FDR) and the colour of each tile corresponds to the row-wise z-score transformed concentrations. In (C-D) the memory time-point is 90-days post-challenge and in (E) memory is 45-days post-challenge.

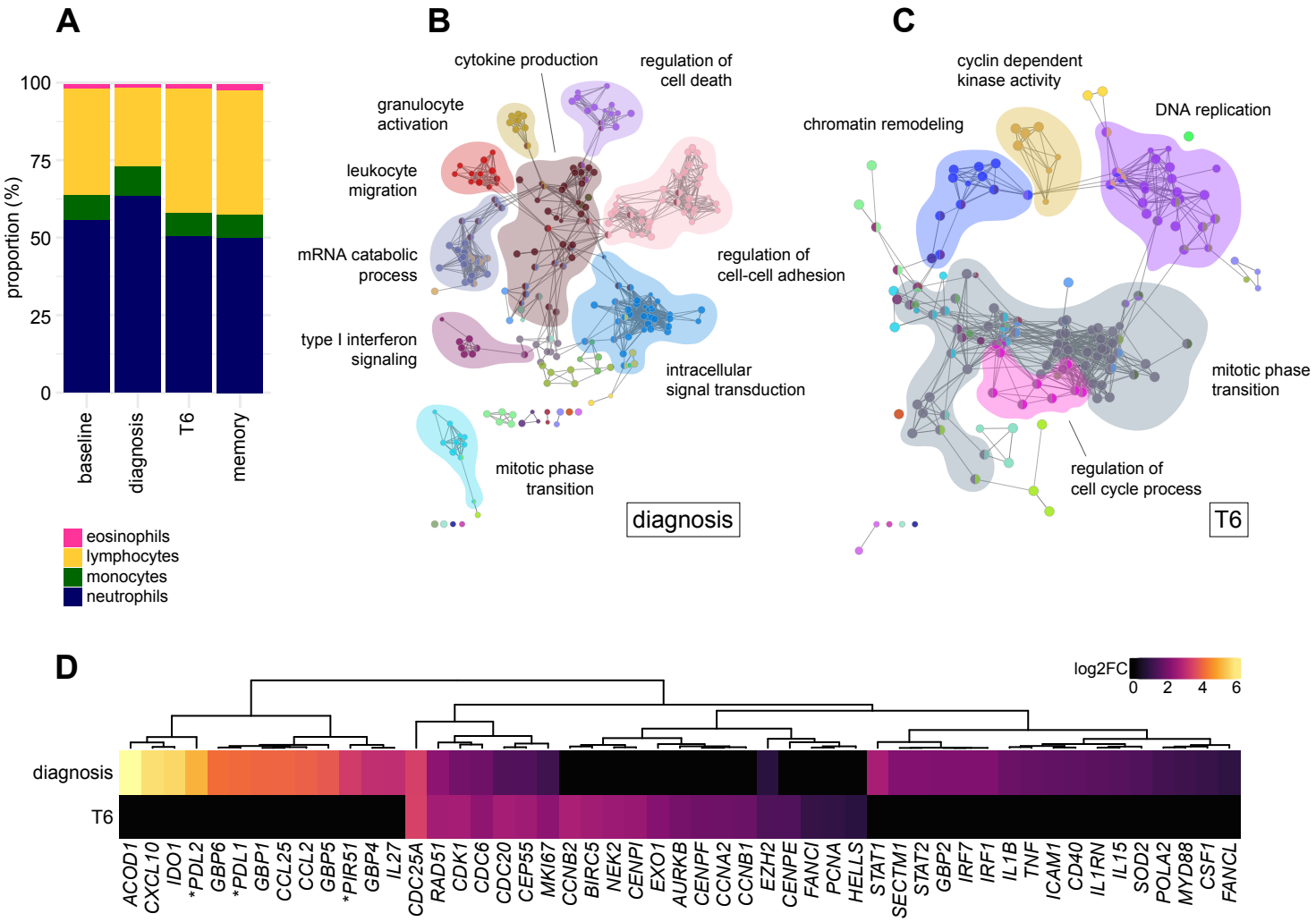
A
100
75
50
25
0
proportion (%)
baseline
diagnosis
T6
memory
eosinophils
lymphocytes
monocytes
neutrophils
B
cytokine production
regulation of cell death
granulocyte activation
leukocyte migration
mRNA catabolic process
regulation of cell-cell adhesion
type I interferon signaling
intracellular signal transduction
mitotic phase transition
diagnosis
C
cyclin dependent kinase activity
DNA replication
chromatin remodeling
mitotic phase transition
regulation of cell cycle process
T6
D
log2FC
0 2 4 6
diagnosis
T6
ACOD1
CXCL10
IDO1
*PDL2
GBP6
*PDL1
GBP1
CCL25
CCL2
GBP5
*PIR51
GBP4
IL27
CDC25A
RAD51
CDK1
CDC6
CDC20
CEP55
MKI67
CCNB2
BIRC5
NEK2
CENPI
EXO1
AURKB
CENPF
CCNA2
CCNB1
EZH2
CENPE
FANCI
PCNA
HELLS
STAT1
SECTM1
STAT2
GBP2
IRF7
IRF1
IL1B
TNF
ICAM1
CD40
IL1RN
IL15
SOD2
POLA2
MYD88
CSF1
FANCL

Figure 2. Inflammation is followed by a transcriptional signature of proliferation. (**A**) Proportion of lymphocytes, monocytes, neutrophils and eosinophils in whole blood at baseline, diagnosis, T6 and 90-days post-challenge (memory). The mean frequency is shown for each time-point (n = 6). Note that the relative increase in abundance of myeloid cells between baseline and diagnosis is 13.6%. (**B**-**C**) Genes that were differentially expressed in whole blood at diagnosis (B) and T6 (C) (relative to baseline, adj $p < 0.05$ and fold-change > 1.5) were used to create a gene ontology network in ClueGO. Each node represents a GO term and node size is determined by enrichment adjusted p value. GO terms that share > 40% of genes are connected by a line and organised into discrete functional groups (each given a unique colour). The major functional groups are highlighted and labelled with a representative GO term. (**D**) The log2 fold-change of signature genes associated with interferon signaling, type I inflammation and proliferation are shown in whole blood at diagnosis and T6 (relative to baseline). Genes are ordered by unsupervised hierarchical clustering (denoted by the dendogram) and those that were not differentially expressed (adj $p > 0.05$) are shown with a fold-change of zero. Asterisks indicate that common gene names have been used. In (B-D) n = 6 per time-point.

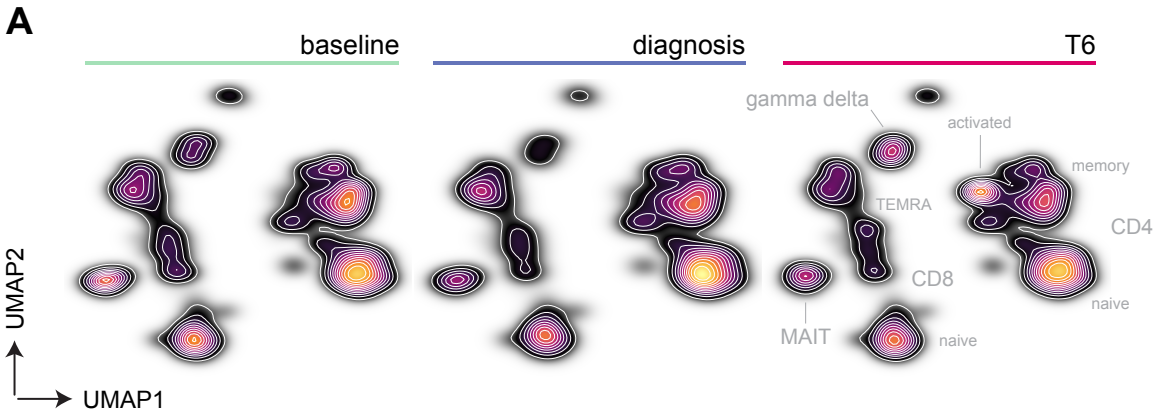
A
baseline
diagnosis
T6
gamma delta
activated
memory
TEMRA
CD4
CD8
naive
MAIT
naive
UMAP2
UMAP1

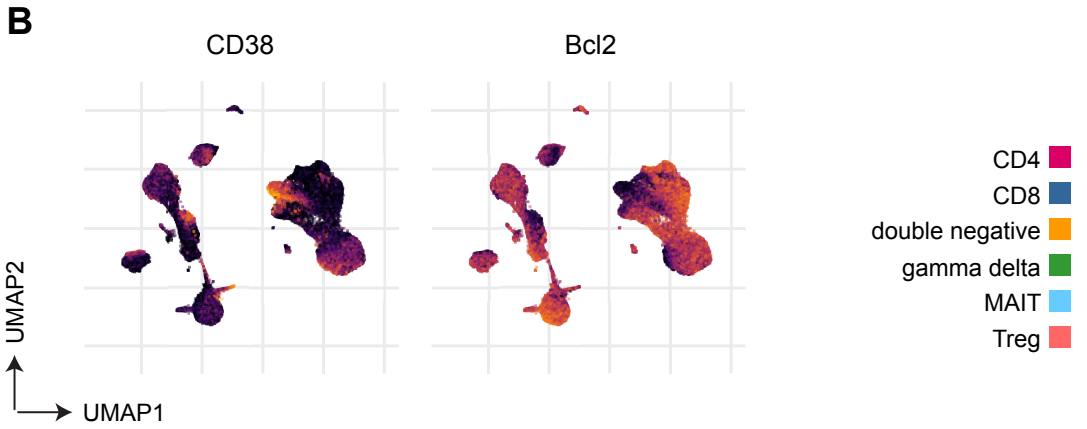
B
CD38
Bcl2
CD4
CD8
double negative
gamma delta
MAIT
Treg
UMAP2
UMAP1

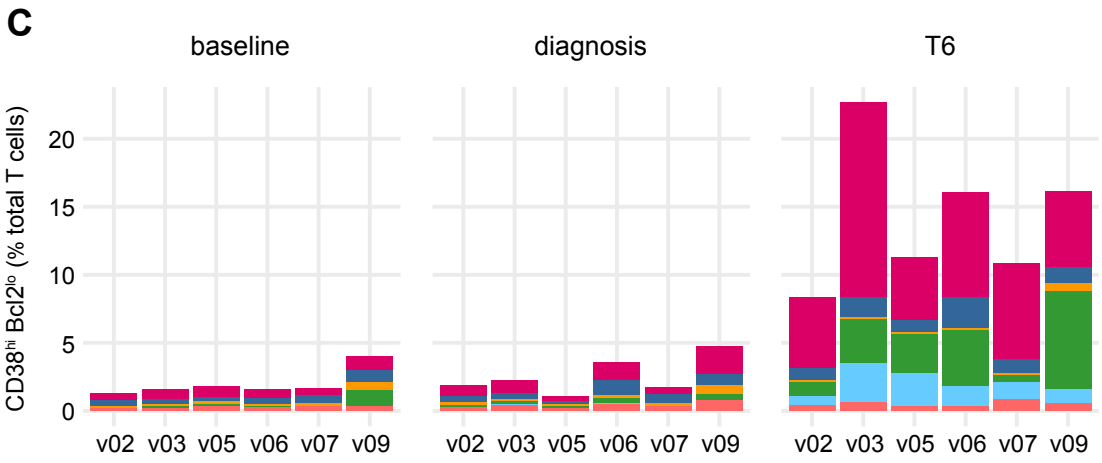
C
baseline
diagnosis
T6
CD38hi Bcl2lo (% total T cells)
0
5
10
15
20
v02 v03 v05 v06 v07 v09
v02 v03 v05 v06 v07 v09
v02 v03 v05 v06 v07 v09

Figure 3. Proliferation coincides with the appearance of activated T cells. Whole blood was preserved within 30-minutes of blood draw at baseline, C10, diagnosis and T6. Samples were stained with a T cell focussed antibody panel (details in Supplemental File 2) and acquired on a Helios mass cytometer. (**A**) UMAP projection coloured by cell density and split by time-point; labels indicating the location of each major T cell subset are shown (refer to Supplemental Figure 1 for the expression of lineage and memory markers). (**B**) Expression of CD38 and Bcl2 across the UMAP projection at T6; each marker is independently scaled for visualisation. In (A-B) data from all volunteers were concatenated and split by time-point (n = 6). (**C**) Stacked bar chart showing the sum of activated ($CD38^{hi}$ $Bcl2^{lo}$) T cells at each time-point; each bar represents one volunteer (n = 6) and bars are colour-coded by lineage.

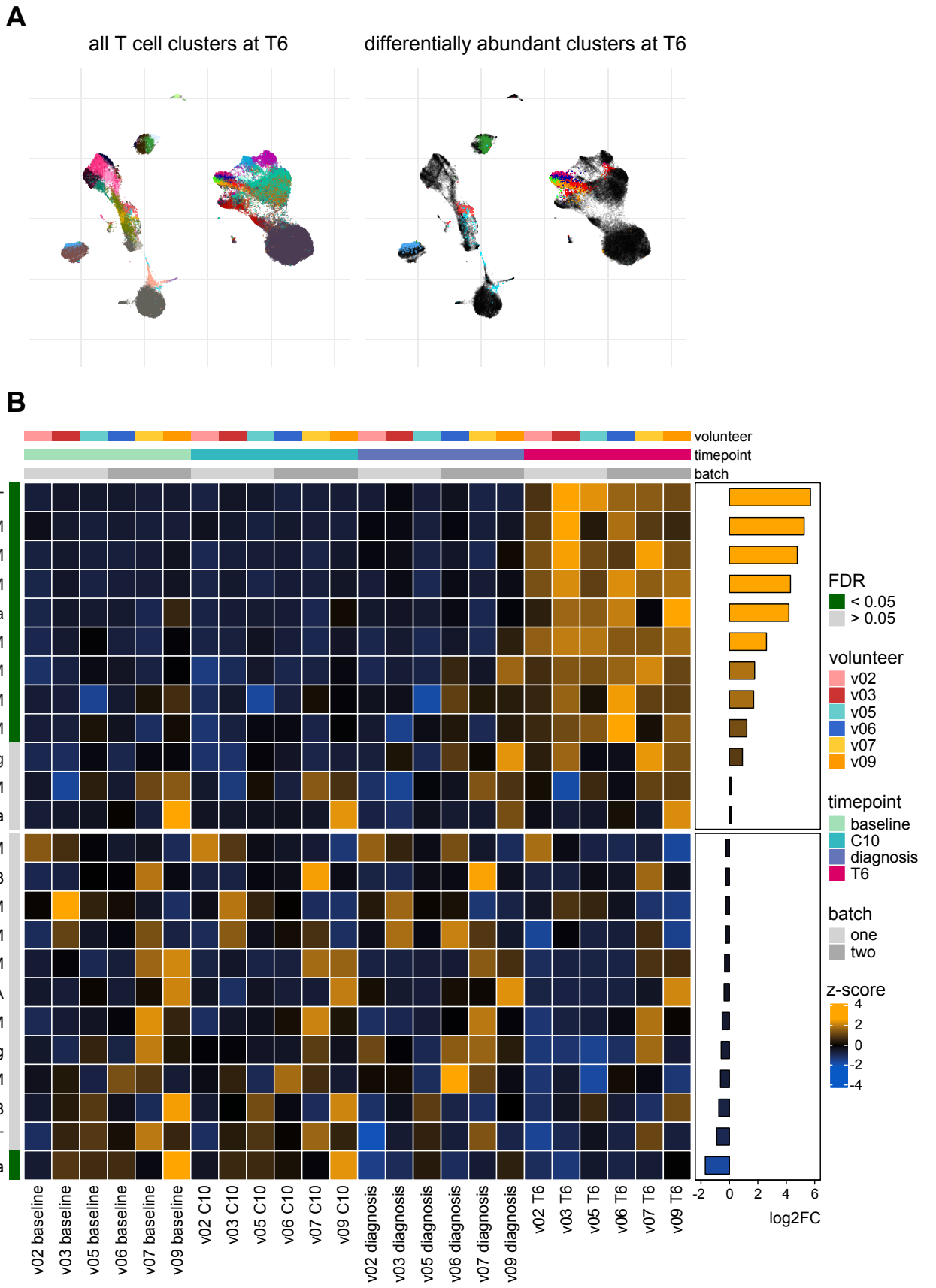
A
all T cell clusters at T6
differentially abundant clusters at T6
B
volunteer
timepoint
batch
activated MAIT
activated CD27- cytotoxic CD4 EM
activated CTLA4+ CD4 EM
activated CD4 EM
activated CD161+ gamma delta
activated CD4 CM
activated HLA-DR- CD4 EM
activated CD8 EM
activated HLA-DR- CD8 EM
activated Treg
PD1+ CD4 EM
CD161- gamma delta
CD27- CD4 EM
CD27- cytotoxic CD8
CD4 CM
CD4 EM
CD8 EM
activated double negative TEMRA
CD57+ CD8 EM
skin-homing Treg
skin-homing CD4 EM
CD28- CD8
MAIT
CD161+ gamma delta
v02 baseline
v03 baseline
v05 baseline
v06 baseline
v07 baseline
v09 baseline
v02 C10
v03 C10
v05 C10
v06 C10
v07 C10
v09 C10
v02 diagnosis
v03 diagnosis
v05 diagnosis
v06 diagnosis
v07 diagnosis
v09 diagnosis
v02 T6
v03 T6
v05 T6
v06 T6
v07 T6
v09 T6
-2
0
2
4
6
log2FC
FDR
< 0.05
> 0.05
volunteer
v02
v03
v05
v06
v07
v09
timepoint
baseline
C10
diagnosis
T6
batch
one
two
z-score
4
2
0
-2
-4

Figure 4. *P. vivax* activates every T cell lineage. (**A**) UMAP projection showing all 34 T cell clusters (left) and those that were differentially abundant at T6 (right) (relative to baseline, FDR < 0.05 and fold-change > 2). Data from all volunteers and time-points were concatenated for clustering, and each cluster has a unique colour. (**B**) Heatmap showing the relative abundance of T cell clusters through time. Each row is a T cell cluster and each column a sample; clusters are ordered by log2 fold-change at T6 (relative to baseline). Only 24 of the 34 T cell clusters are shown (those with the lowest FDR) and tiles are coloured according to row-wise z-scores of (arcsine square root transformed) cluster frequencies. In (A-B) n = 6 per time-point.

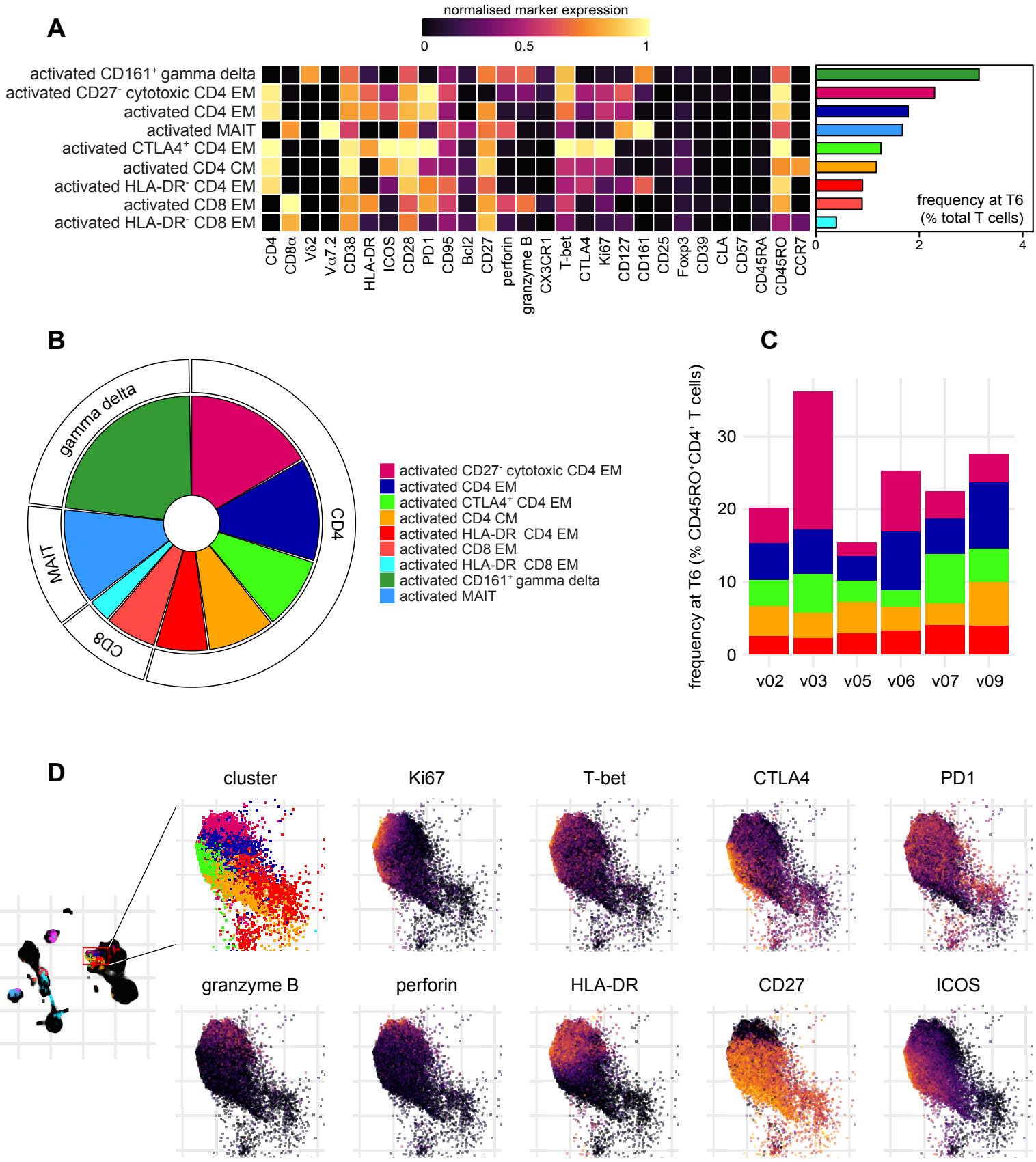
A
normalised marker expression
0
0.5
1
activated CD161+ gamma delta
activated CD27- cytotoxic CD4 EM
activated CD4 EM
activated MAIT
activated CTLA4+ CD4 EM
activated CD4 CM
activated HLA-DR- CD4 EM
activated CD8 EM
activated HLA-DR- CD8 EM
CD4
CD8α
Vδ2
Vα7.2
CD38
HLA-DR
ICOS
CD28
PD1
CD95
Bcl2
CD27
perforin
granzyme B
CX3CR1
T-bet
CTLA4
Ki67
CD127
CD161
CD25
Foxp3
CD39
CLA
CD57
CD45RA
CD45RO
CCR7
frequency at T6
(% total T cells)
0
2
4
B
gamma delta
CD4
CD8
MAIT
activated CD27- cytotoxic CD4 EM
activated CD4 EM
activated CTLA4+ CD4 EM
activated CD4 CM
activated HLA-DR- CD4 EM
activated CD8 EM
activated HLA-DR- CD8 EM
activated CD161+ gamma delta
activated MAIT
C
frequency at T6 (% CD45RO+CD4+ T cells)
0
10
20
30
v02
v03
v05
v06
v07
v09
D
cluster
Ki67
T-bet
CTLA4
PD1
granzyme B
perforin
HLA-DR
CD27
ICOS

Figure 5. Activated T cells are functionally heterogeneous. (**A**) Heatmap showing normalised median expression values of all markers used for clustering in each of the 9 T cell clusters that were differentially abundant at T6. The horizontal bar chart shows the average frequency of each cluster across all volunteers. (**B**) Pie showing the relative size of each differentially abundant T cell cluster at T6. (**C**) Stacked bar chart showing the sum of activated $CD4^+$ T cells at T6; each bar represents one volunteer. Data are shown as a proportion of the total non-naive $CD45RO^+$ $CD4^+$ T cell pool. (**D**) UMAP projection showing the expression of activation, proliferation and differentiation markers across each of the $CD4^+$ T cell clusters that were differentially abundant at T6; each marker is independently scaled using arcsine transformed signal intensity. The expression of these markers is shown across the entire UMAP projection in Supplemental Figure 5. In (A-D) n = 6 and T cell clusters are colour-coded according to the legend in (B).

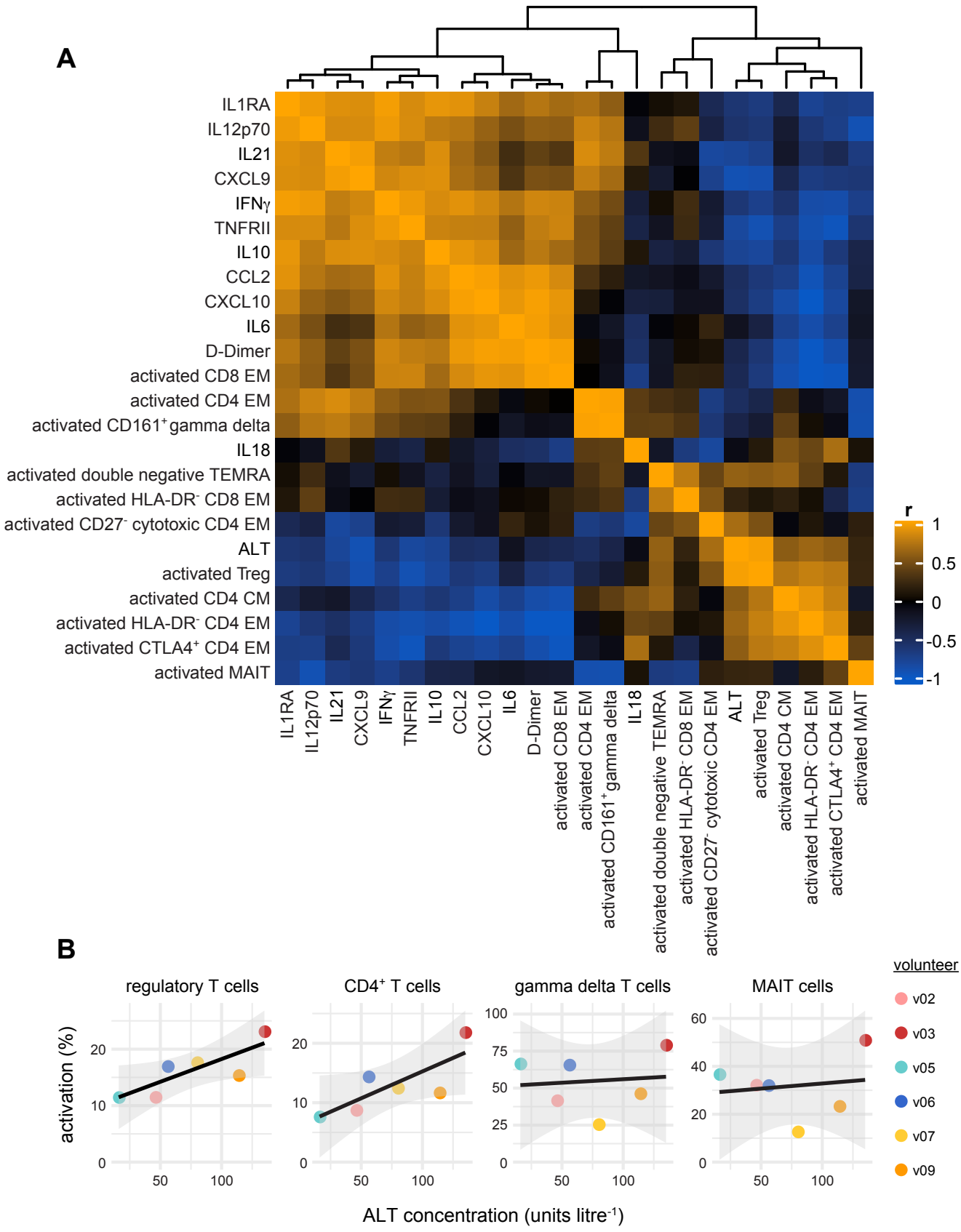
A
IL1RA
IL12p70
IL21
CXCL9
IFNγ
TNFRII
IL10
CCL2
CXCL10
IL6
D-Dimer
activated CD8 EM
activated CD4 EM
activated CD161+ gamma delta
IL18
activated double negative TEMRA
activated HLA-DR- CD8 EM
activated CD27- cytotoxic CD4 EM
ALT
activated Treg
activated CD4 CM
activated HLA-DR- CD4 EM
activated CTLA4+ CD4 EM
activated MAIT
r
1
0.5
0
-0.5
-1
B
regulatory T cells
CD4+ T cells
gamma delta T cells
MAIT cells
activation (%)
ALT concentration (units litre-1)
volunteer
v02
v03
v05
v06
v07
v09

Figure 6. T cell activation is independent of systemic inflammation. (**A**) Heatmap showing a Pearson correlation matrix of the log2 transformed fold-change of each activated T cell cluster and the twelve most variable plasma analytes (FDR < 0.05). The fold-change was calculated either at diagnosis or T6 (relative to baseline) according to when this was largest for each feature. The absolute concentration of plasma ALT at T6 (the peak of the response) is also included. The order of features was determined by hierarchical clustering and the associated dendrogram is shown at the top of the heatmap. (**B**) Correlation between ALT concentration and the frequency of activated ($CD38^{hi}$ $Bcl2^{lo}$) T cells at T6. Note that innate-like and adaptive T cell clusters belonging to the same lineage were merged to analyse their relationship with collateral tissue damage at a subset level. Loess regression line is shown in black and the 95% confidence intervals in grey. In (A-B) n = 6 per time-point.

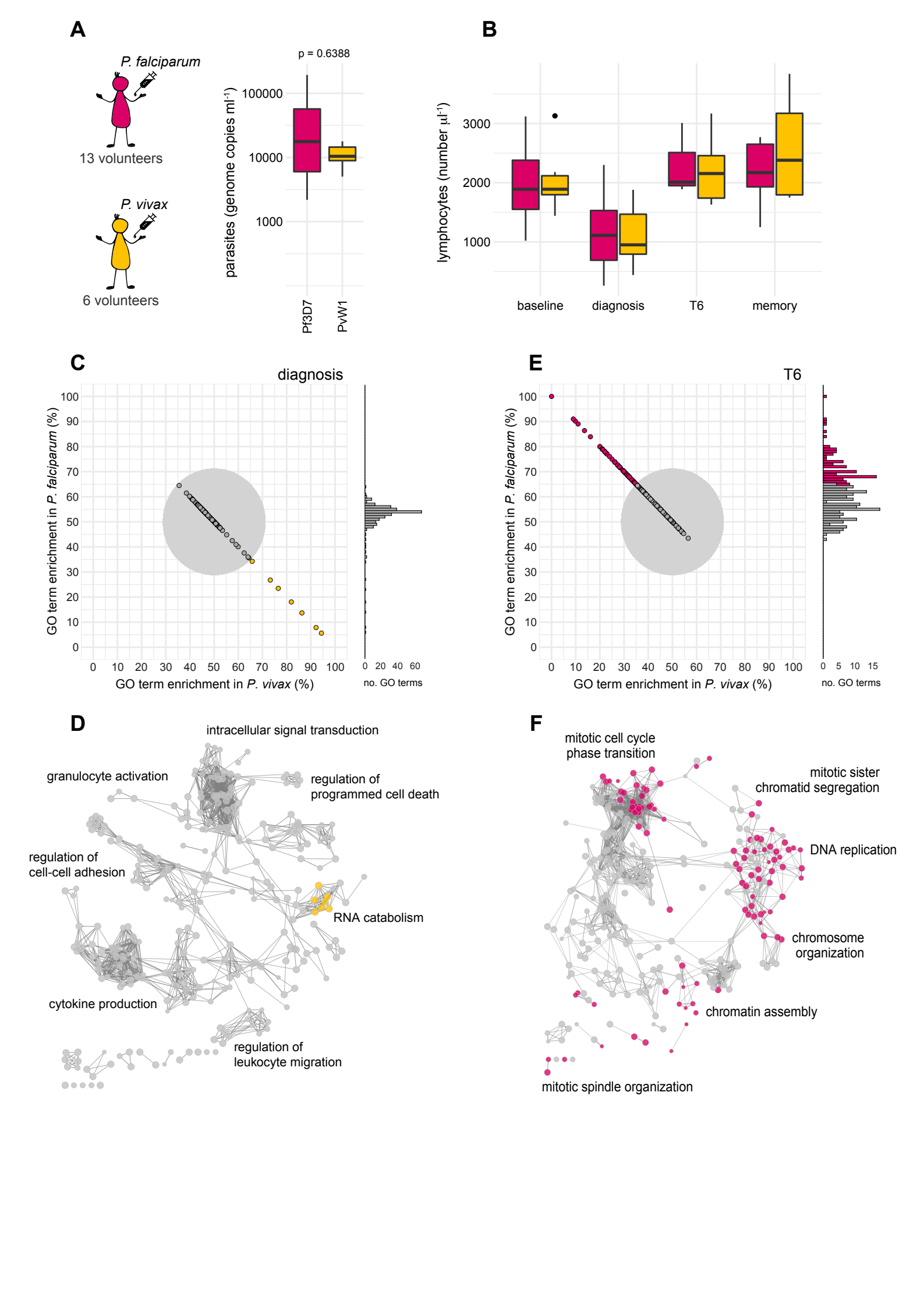
A
P. falciparum
13 volunteers
P. vivax
6 volunteers
p = 0.6388
parasites (genome copies ml-1)
100000
10000
1000
Pf3D7
PvW1
B
lymphocytes (number µl-1)
3000
2000
1000
baseline
diagnosis
T6
memory
C
diagnosis
GO term enrichment in P. falciparum (%)
GO term enrichment in P. vivax (%)
no. GO terms
E
T6
GO term enrichment in P. falciparum (%)
GO term enrichment in P. vivax (%)
no. GO terms
D
intracellular signal transduction
granulocyte activation
regulation of programmed cell death
regulation of cell-cell adhesion
RNA catabolism
cytokine production
regulation of leukocyte migration
F
mitotic cell cycle phase transition
mitotic sister chromatid segregation
DNA replication
chromosome organization
chromatin assembly
mitotic spindle organization

Figure 7. The host response is shaped by parasite species. (**A**) The maximum circulating parasite density in each volunteer during the VAC063/VAC063C CHMI trials (*P. falciparum*) and the VAC069A study (*P. vivax*). Significance between parasite species was assessed by Wilcoxon rank sum exact test (two-tailed). (**B**) The total number of circulating lymphocytes through infection and convalescence; the memory time-point is 90-days post-challenge. In (A-B) box (median and IQR) and whisker (1.5x upper or lower IQR) plots are shown with outliers as dots; n = 13 for *P. falciparum* and n = 6 for *P. vivax* (except at T6 where n = 3 for *P. falciparum*). (**C**-**F**) Whole blood RNA-sequencing was performed identically during the VAC063/VAC063C and VAC069A studies and lists of differentially expressed genes (adj $p < 0.05$ and fold-change > 1.5) were combined for GO analysis at diagnosis and T6. Importantly, for every GO term the fraction of associated genes derived from each volunteer cohort was retained. (C and E) Each GO term is represented by a single point and these are positioned according to the proportion of genes that were differentially expressed in volunteers infected with *P. falciparum* or *P. vivax*. The grey circle represents a 65% threshold that needed to be crossed to call a GO term as majoritively derived from one volunteer cohort; beyond this threshold GO terms are coloured by enrichment as shown in (A). (D and F) ClueGO networks reveal the functional organisation of GO terms at diagnosis (D) and T6 (F); nodes are colour-coded by enrichment (shared GO terms are shown in grey) and each of the major functional groups is labelled with a representative GO term. In (C-D) n = 13 for *P. falciparum* and n = 6 for *P. vivax* and in (E-F) n = 3 and 6, respectively.

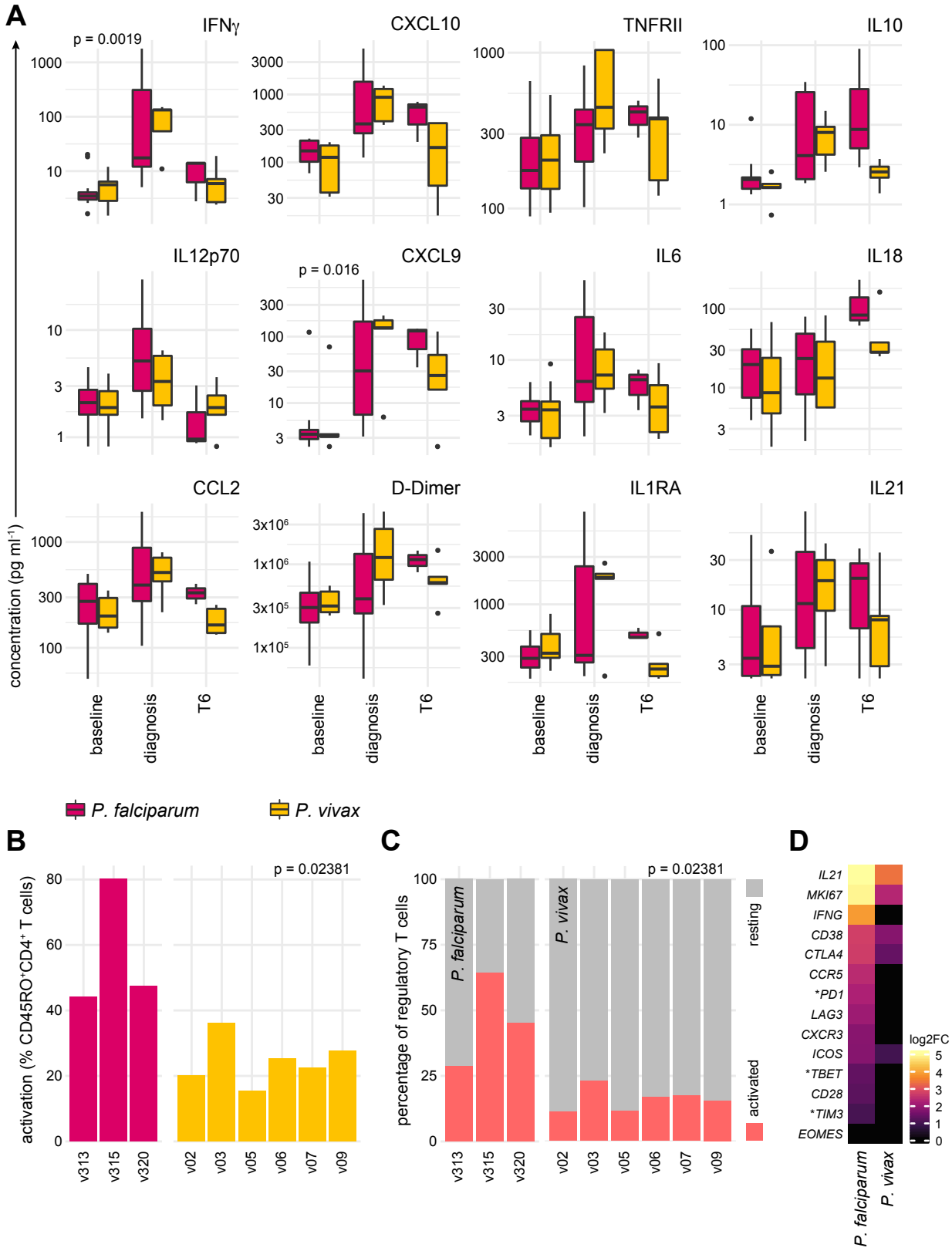
A
IFNγ
p = 0.0019
CXCL10
TNFRII
IL10
IL12p70
CXCL9
p = 0.016
IL6
IL18
CCL2
D-Dimer
IL1RA
IL21
concentration (pg ml-1)
baseline
diagnosis
T6
P. falciparum
P. vivax
B
activation (% CD45RO+CD4+ T cells)
p = 0.02381
v313
v315
v320
v02
v03
v05
v06
v07
v09
C
percentage of regulatory T cells
p = 0.02381
resting
activated
D
IL21
MKI67
IFNG
CD38
CTLA4
CCR5
*PD1
LAG3
CXCR3
ICOS
*TBET
CD28
*TIM3
EOMES
log2FC

Figure 8. Parasite species regulates T cell activation and differentiation. (**A**) Multiplexed plasma analytes were measured in the VAC063/VAC063C and VAC069A CHMI studies using a custom Legendplex assay. Linear regression was used to identify analytes that vary significantly between volunteer cohorts at diagnosis and/or T6 (relative to baseline). After correcting for multiple comparisons (Benjamini-Hochberg) only 2 of 39 analytes were significant (adj $p < 0.05$ at diagnosis). The twelve plasma analytes shown all varied significantly through time in *P. vivax* infected volunteers (as shown in Figure 1E). Box (median and IQR) and whisker (1.5x upper or lower IQR) plots are shown with outliers as dots; n = 12 for *P. falciparum* at baseline/diagnosis and n = 3 at T6; n = 5 for *P. vivax* at all time-points. Note that samples from v1040 (VAC063) and v09 (VAC069A) were excluded after failing QC. (**B**-**C**) The proportion of non-naive $CD45RO^{+}$ $CD4^{+}$ T cells (B) and regulatory T cells (C) activated ($CD38^{hi}$ $Bcl2^{lo}$) at T6 in volunteers infected with *P. falciparum* or *P. vivax*. FlowSOM was used to identify activated T cell clusters independently in each volunteer cohort and the frequency of activated clusters were summed; each bar represents one volunteer. Significance between parasite species was assessed by Wilcoxon rank sum exact test (two-tailed). (**D**) Heatmap of signature T cell genes showing their log2 fold-change at T6 (relative to baseline) in whole blood analysed by RNA-sequencing; n = 3 for *P. falciparum* and n = 6 for *P. vivax*. Asterisks indicate that common gene names were used and genes that were not differentially expressed (adj $p > 0.05$) are shown with a fold-change of zero.